Orographic Influences on Precipitation in a Continental Mountain Environment as Observed by Mountain and Valley Profiling Radars

Michael L. Wasserstein,[a] Ashley N. Evans,[a] Peter G. Veals,[a] David E. Kingsmill[b], and W. James Steenburgh[a]

[a]*Department of Atmospheric Sciences, University of Utah, Salt Lake City, Utah*

[b]*Cooperative Institute for Research in Environmental Sciences, University of Colorado Boulder, Boulder, Colorado*

Corresponding author: Michael L. Wasserstein, michael.wasserstein@utah.edu

ABSTRACT

Orography has a dramatic influence on cool-season precipitation, building an upper-elevation snowpack for regional water resources and winter tourism and modulating winter storms that impact transportation and public safety. Using K-band profiling Micro Rain Radar (MRR) observations from the Wasatch Mountains (2682 m MSL) and the adjoining Salt Lake Valley (1372 m MSL), this paper investigates the characteristics of cool-season storms in a continental mountain environment of the eastern Great Basin of North America. Compared to the valley site, the mountain site observed a higher frequency of low-level reflectivity ≥ 5 dBZ_e, consistent with greater precipitation frequency due to orographic enhancement. Echoes were deepest during southerly or southwesterly flow with high integrated vapor transport and the passage of cold fronts or baroclinic troughs and shallowest during northwesterly flow post-cold-frontal periods when median -10 dBZ_e echo tops were only 1260 m AGL. During post-cold-frontal periods, reflectivities most often increased with decreasing height near the ground at the mountain site, whereas other storm types featured nearly equal frequencies of increasing and decreasing reflectivity with decreasing height. Due to presumed sub-cloud sublimation and evaporation, post-cold-frontal periods at the valley site featured decreasing modal reflectivity with decreasing height near the ground. These results illustrate important contrasts in precipitation growth and loss processes between mountain and lowland sites, where sub-cloud sublimation and evaporation represent underappreciated mechanisms for reducing lowland precipitation and enhancing the orographic precipitation gradient. Operational and spaceborne precipitation radars likely inadequately sample these near-surface processes in continental mountain environments.

SIGNIFICANCE STATEMENT

Mountains strongly affect winter storms, complicating forecasting and enabling the development of an upper-elevation snowpack that is vital for water resources and winter tourism. This research shows that contrasts in valley and mountain precipitation in drier, continental mountain environments are strongly influenced by shallow processes near the ground, which are poorly sampled by conventional weather radars and satellites. In the mountains, precipitation growth can occur near the ground, especially in post-cold-frontal environments, whereas valley precipitation can decrease as it falls through a dry layer. The latter is an underappreciated contributor to the mean increase of precipitation with elevation found in continental mountain environments.

1. Introduction

Orographic precipitation contributes to some of the world's prominent climatological and ecological gradients and causes geophysical hazards such as avalanches, floods, and landslides (Roe 2005; Houze 2012; Meyers and Steenburgh 2013). A disproportionate fraction of the world's runoff and freshwater resources originate from mountainous regions (Meybeck et al. 2001; Viviroli and Weingartner 2004; Viviroli et al. 2007) and, in the western United States, snowmelt contributes to between 50% and 70% of the total runoff (Li et al. 2017). Synoptic-scale storms and orographic enhancement processes during the cool season generate much of this snow (Houze 2012; Koszuta et al. 2024).

In the Great Basin of North America, Salt Lake City, Utah exemplifies the importance of freshwater resources derived from orographic precipitation and snowmelt for an urban mountain community. Salt Lake City is part of the rapidly growing Salt Lake Valley, with more than 1 million residents at the western base of the Wasatch Mountains (hereafter Wasatch; Fig. 1; Utah Department of Transportation 2022a). Roughly 50–60% of the city's water comes from four creeks that issue from the central Wasatch (Bardsley et al. 2013). The region features dramatic climatological gradients of precipitation with elevation, and much of the runoff in these creeks originates as snowmelt at upper elevations. Mean cool-season (Nov–Apr) liquid precipitation equivalent (LPE) increases from 238 mm at Salt Lake City International Airport (KSLC; 1288 m MSL) in the Salt Lake Valley to 813 mm at Alta (2655 m MSL) in the central Wasatch, where most of the cool-season precipitation falls as snow (Fig. 1b; NCEI 2021). Heavy snowfall and avalanches are common in the Wasatch, particularly in Little Cottonwood Canyon, a popular destination for outdoor recreation. During the record-setting 2022/23 cool season, which produced 2294 cm of snow in upper Little Cottonwood Canyon, 98 avalanches hit SR-210, the road that winds up Little Cottonwood Canyon, resulting in 10 full-day road closures and food shortages (Utah Department of Transportation 2022b; Jag 2023; Alta Ski Area 2023; Wasserstein and Steenburgh 2024, hereafter WS24). Compounding the natural geophysical hazards present in the Wasatch, beam blockage limits the ability of the local mountaintop NEXRAD WSR-88D radar to detect precipitation, posing challenges to forecasting and roadway management in Little Cottonwood Canyon (Wood et al. 2003).

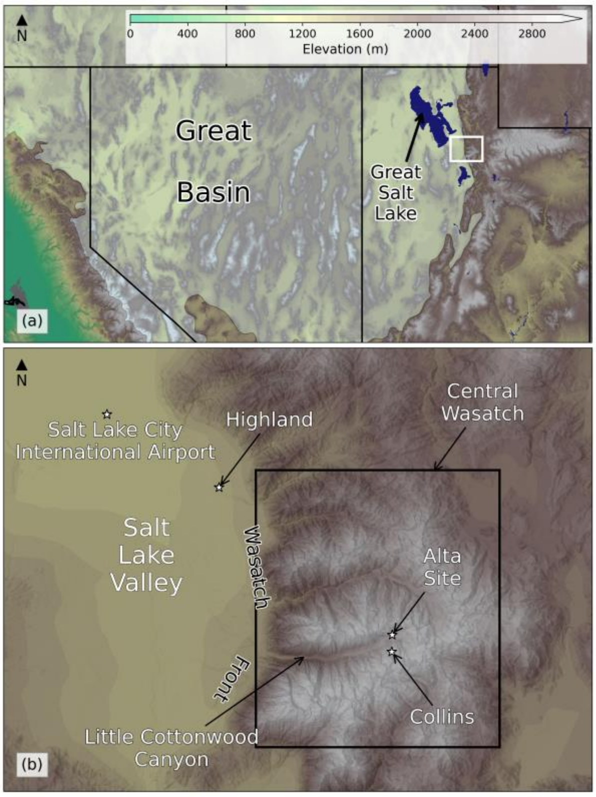

Fig. 1. Topography of (a) the Great Basin (m; scale at top) and (b) the study region in northern Utah [identified by the white box in (a)] with key geographic features annotated. The black box in (b) outlines the central Wasatch.

Winter storms can also have substantial impacts at lower elevations, such as along the densely populated Wasatch Front. Orographic precipitation research has often concentrated primarily on processes that enhance precipitation at upper elevations (e.g., Houze 2012) or the upstream lowlands where topographic blocking can lead to ascent and precipitation upstream of the mountain slope (Neiman et al. 2002; Medina and Houze 2003; Abel et al. 2009; Ackermann et al. 2021). Although this effect has been documented upstream of the northern Wasatch (Cox et al. 2005), the presence of upstream mountain barriers disrupts the potential for blocking front formation in the Salt Lake Valley.

Less commonly investigated are mechanisms that may lead to precipitation losses over lowland areas, namely sublimation and evaporation within dry airmasses often resident in valleys in continental mountain environments (Stoelinga et al. 2013). Such sublimation or evaporation leads to a decrease in precipitation with distance below cloud base, enhancing the orographic precipitation gradient (Steenburgh 2003; Schultz and Trapp 2003). Spatial variations in the depth and saturation deficit of dry airmasses in lowland areas exacerbate the challenges of precipitation and snowfall forecasting. Such effects are underappreciated and rarely investigated, raising questions concerning their significance for the cool-season hydroclimate of mountainous regions and their influence on lowland precipitation.

This research uses two cool seasons of vertically pointing radar observations from a mountain site in upper Little Cottonwood Canyon and a site in the adjoining valley to examine the characteristics of winter storms at varying elevations. Vertically pointing radars have proven valuable to study orographic and winter storms in the European Alps (Kneifel et al. 2011,2022; Hagen et al. 2022), Tibetan Plateau (Xu et al. 2023), Great Lakes of North America (Pettersen et al. 2020), and Pacific Northwest (Cunningham and Yuter 2014). The use of mountain and valley radars enables insight into the processes affecting orographic precipitation gradients in this continental mountain environment. Such an approach has been used to examine orographic influences on storms in other regions. For example, Hardin et al. (2011) used mountain–valley vertically pointing radars to illustrate an increase in echo top heights from the valley to mountain crest in Colorado's Park Range, and Ackermann et al. (2021) used three vertically pointing radars to examine the evolution of storms in Australia's Snowy Range during blocked and unblocked periods. Minder et al. (2015) used four radars to describe the convective-to-stratiform transition and increase in echo persistence over the Tug Hill Plateau during lake-effect storms.

In the next section we describe the data and methods used, including site characteristics and diagrams used to examine the data. In section 3 we present a summary of the data characteristics during the two cool seasons and examine how valley and mountain radar profiles vary with synoptic storm type, including differences between deep storms associated with elevated integrated vapor transport (IVT) from the south or southwest, frontal passages, and shallow post-cold-frontal periods. We conclude with a summary of results and their implications for understanding and measurement of precipitation in continental mountain environments.

2. Data and methods

a. Research sites

We operated two Metek vertically pointing K-band Micro Rain Radar 2s (hereafter MRR) and first-generation OTT PARSIVEL disdrometers (hereafter PARSIVEL) during the 2022/23 and 2023/24 cool seasons at the Alta and Highland observing sites (Fig. 1b; Veals et al. 2025; Steenburgh et al. 2025a,b,c). The Alta site was in upper Little Cottonwood Canyon in the central Wasatch (2682 m MSL), on a platform approximately 5.5 m AGL, as necessitated by the deep seasonal snowpack (Fig. 2a). We installed the MRR and PARSIVEL on the roof of Highland in the Salt Lake Valley (1372 m MSL), 23 km northwest of Alta (Figs. 1b;2a). We chose Highland because it is located directly upstream of Alta during northwest flow, a favored flow direction for heavy snowfall at Alta (WS24).

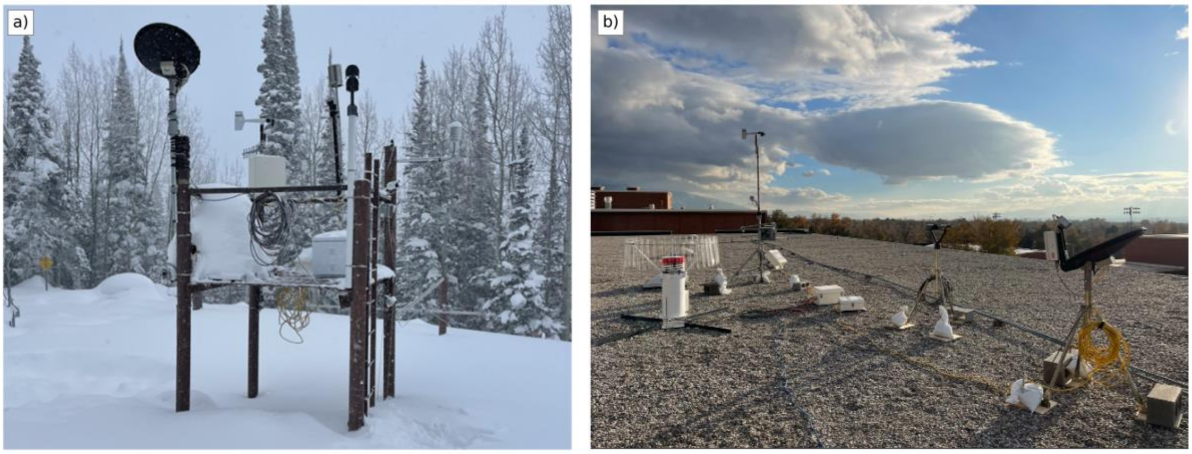

Fig. 2. Images of (a) the Alta site with the MRR and PARSIVEL mounted on the left and right sides of the platform, respectively and (b) the Highland site on the roof of Highland High School with PARSIVEL at center and MRR at right.

b. MRR

The MRR is a vertically profiling continuous-wave Doppler radar that measures spectral power backscatter intensity and creates vertical profiles from hydrometeor diameter and assumed drop-size distributions (Maahn and Kollias 2012; hereafter MK12). The MRRs operate at a 24-GHz frequency with a 1.24-cm wavelength (K–band) and a two-degree beam width (Minder et al. 2015; Pettersen et al. 2020). To increase the MRR sensitivity and allow for better snowfall measurements, we used a postprocessing algorithm designed by MK12 to improve snowfall retrievals by refining sensitivity, noise removal, and velocity dealiasing. This algorithm, which has been used for other snow studies (Minder et al. 2015; Pettersen et al. 2020), enables the retrieval of equivalent radar reflectivity factor, Z_e, Doppler radial velocity, V_r, and spectral width, *SW*. The enhanced retrieval of reflectivity extends the range of detectable precipitation to as low as -14 dBZ_e (MK12; Minder et al. 2015).

We equipped the MRRs with factory heaters to prevent snow and ice accumulation on the dish. At Alta, we also placed heat tape along the edges of the dish and mounting post to minimize icicle formation. Over the 2022/23 season, some snow accumulation occurred on the dish during cold, heavy snowfall periods. For the 2023/24 season, we replaced the dish, as we found the heating coils had separated from the dish surface. This helped, but during events with snowfall rates exceeding 5–7.5 cm h^{-1}, the heater was often unable to prevent snow accumulation on the dish. Using webcam images of the MRRs saved every 5 minutes, we determined that during 1.4% of all periods the MRR dish was covered by snow or ice. We recalculated all statistics after eliminating periods with dish coverage and the results were not qualitatively different. Therefore, for completeness, we display results from all periods with available data.

We collected data at each site using 32 range gates, alternating temporally between 30 and 180-m vertical resolutions. The MRR outputs data every minute, with each minute alternating between 30 and 180-m data. The 180-m range-gate configuration provided lower resolution profiles to 5580 m AGL, and the 30-m configuration provided higher resolution to 930 m AGL. We eliminated the lowest three range gates due to near field effects, and we omitted the highest gate, which often exhibits noise, leaving 27 usable gates (MK12; Minder et al. 2015; Pettersen et al. 2020).

We deployed the MRRs during the fall and removed them during the summer to prevent wear. We performed a neighborhood comparison study with the MRRs at Alta prior to the 2023/24 deployment to test for biases between instruments. During this period, the two MRRs were located ~125 m apart and there was a ~20-m elevation difference between them. This comparison observed three precipitation events and differences between the instruments were $\lesssim$ 2 dBZ_e for Z_e, $\lesssim$ 0.3 m s^{-1} for V_r, and $\lesssim$ 0.15 m s^{-1} for SW (Evans 2025).

Throughout the duration of observations, multiple data outages occurred at Alta, due to heavy snowfall which resulted in power outages and limited access due to avalanche hazard and highway closures. Our analysis focuses on periods with data availability from both MRRs (Table 1). We examine distinct 12-h periods over the two-cool-season study period because we use 12-h manual observations of new snow and LPE taken at 0400 and 1600 LST (1000 or 1100 UTC and 2200 or 2300 UTC, depending on daylight savings) to determine periods during which snow fell (see section 2g for further discussion of these observations).

We require a minimum of 355 observations (of 360 possible observations) during a 12-h period to define a full coverage period which we focus analysis on.

Start Time	End Time (UTC)
1100 UTC 23 Nov 2022	1100 UTC 24 Nov 2022
1100 UTC 25 Nov 2022	1100 UTC 6 Dec 2022
1100 UTC 11 Dec 2022	1000 UTC 29 Mar 2023
1000 UTC 14 Apr 2023	1000 UTC 15 Apr 2023
1000 UTC 16 Apr 2023	1000 UTC 18 Apr 2023
1000 UTC 24 Apr 2023	2200 UTC 24 Apr 2023
1100 UTC 23 Nov 2023	2200 UTC 21 Mar 2024
1000 UTC 23 Mar 2024	1000 UTC 1 May 2024

Table 1. Periods during the two cool seasons with sufficient data available at both observing sites.

c. PARSIVEL

The PARSIVEL uses an optical sensor to measure precipitation fall velocities and diameter (Löffler-Mang and Joss 2000; Löffler-Mang and Blahak 2001). The optical sensor produces a sheet of light through which precipitation particles fall, temporarily reducing the voltage of the signal produced by a photodiode receiver. The magnitude of this voltage reduction is directly related to the along sheet laser cross section of a particle, and the duration of the voltage reduction enables a fall velocity estimate (Löffler-Mang and Joss 2000). The PARSIVEL bins precipitation particles into one of 32 unique velocity bins and size bins, yielding a 32x32 matrix with 1024 possible velocity-size bins.

We produced accumulated matrices of fall velocity and size during the 2022/23 and 2023/24 cool seasons. Following Yuter et al. (2006), we only analyze particles in the size bins >1 mm in diameter, which prevents misclassification of precipitation as small ice particles in mixed precipitation and eliminates the first eight size bins. We use empirically derived size-velocity relationships (Berry and Pranger 1974; Locatelli and Hobbs 1974) and a fall speed density correction (Foote and Toit 1969) to produce lines on the matrices for rain, graupel, and dendrites. The PARSIVEL produces raw data files for each hour it records precipitation with ten-second temporal resolution within each file. Thus, during a period where precipitation was observed for the entire hour, there would be one matrix of data for each 10-second period or 360 total matrices in a 1-h data file. We require a minimum of 150 matrices of data for each raw data file, meaning that 150 of 360 possible 10-second periods featured precipitation. For consistency in our analysis, we only use PARSIVEL data during periods where MRR data was available at both sites (Table 2).

Despite the success of some studies for snow, the PARSIVEL is made for warm precipitation and has been shown to underestimate fall speed and overestimate the number of small snowflakes and large particles (Battaglia et al. 2010). As snow aggregates fall, they can follow complex trajectories including spinning, spiraling, and shaking (Lew et al. 1986), which could influence fall velocities in the PARSIVEL. Graupel can occasionally hit the PARSIVEL sensor head and bounce into the beam, not giving a true representation of the graupel terminal velocity. If only part of a precipitation particle intersects the PARSIVEL beam, the sensor can record a particle falling too fast or underestimate the particle size (Yuter et al. 2006). After careful analysis of the PARSIVEL data, we found considerable wind-related artifacts in the Alta data that made it difficult to unambiguously distinguish real data from artifacts, so we elected to only present data from Highland in this paper.

d. CFADs

We analyzed the distributions of the MRR data using contoured frequency by altitude diagrams (hereafter CFADS; Yuter and Houze 1995), where we show height on the ordinate and Z_e, V_r, or *SW* on the abscissa. The bin heights correspond to the range-gate interval, with 30-m range-gate data used up to 810 m AGL (i.e., the highest 30-m range gate is centered at 810 m AGL and extends from 795 to 825 m AGL) and 180-m data used from 900 m AGL and above. We combined the 30 and 180-m CFADs to limit figures and ease the analysis of storm characteristics aloft and near the surface. This results in an overlap of 15 m in the top half of the last 30-m range gate and the bottom of the first 180-m gate, which extends from 810 to 990 m AGL, leaving the latter slightly smaller (165 m) than the other 180-m bins for presentation purposes. In our analyses, a small discontinuity in statistics occasionally appears near the transition from the 30- to 180-m range gates, and we provide an explanation for the discontinuity in appendix A; this small discontinuity does not qualitatively impact our results. We normalized the CFADs by dividing the number of observations in each height bin by the total number of observations at the corresponding height and converting to a percentage, so that the sum of all frequencies at each height is 100%. For all CFADs, we only display data for height bins that have ≥20% of the observations of the height bin with the maximum number of observations, which eliminates high frequency values which would otherwise occur due to a lack of observations. Overlaid on these plots are the 25th, 50th, and 75th percentiles at each range gate. We note that data from the 30- and 180-m range-gate intervals are not collected simultaneously as each radar alternates between the two range-gate resolutions every minute.

e. Reflectivity Profiles

We further analyzed the MRR data by producing time-normalized vertical profiles of the frequency of $Z_e \geq 5$ dBZ$_e$. We normalized these profiles by dividing the frequency of $Z_e \geq 5$ dBZ$_e$ at each height by the total number of times contained in the dataset, regardless of if the MRR recorded reflectivity values or not. Thus, the normalization used here contains profiles where no Z_e values were recorded, whereas the normalization used for CFADs only normalizes by the number of instances where Z_e was recorded in each height bin. Using time normalization allows us to directly compare how often reflectivity was observed during storms at Alta and Highland, providing different information compared to statistics in the CFADs. We chose 5 dBZ$_e$ because it represents a water equivalent snowfall rate of ~.2 mm h^{-1}, just below the standard for measurable precipitation in the US [.25 mm h^{-1} (.01 in h^{-1})] based on the Z–S relationship of Matrosov (2007), which has been used in other profiling radar studies (e.g., Kneifel et al. 2011; MK12; Pettersen et al. 2020).

f. Vertical Reflectivity Gradient

To determine variations in MRR Z_e with height we examined the vertical reflectivity gradient (VRG), which is calculated as

$$\mathrm{VRG} = \frac{\sum_{i=1}^{n}(z_i - \bar{z})(Z_{e,i} - \bar{Z}_e)}{\sum_{i=1}^{n}(z_i - \bar{z})^2}, \qquad (1)$$

where n represents the total number of range gates in a layer depth and z is the range-gate height. Equation (1) calculates the VRG using linear regression, where negative values indicate increasing Z_e toward ground and positive values indicate decreasing Z_e toward ground. In the results shown in this paper, the layer depth uses data from 30-m range gates from 120 to 900 m AGL, which represents the low-level change in reflectivity with height. We display histograms of VRG, and for instances with no recorded reflectivity at the top and/or bottom of the layer depth, we include frequencies on a bar chart adjacent to the histograms.

g. Seasonal statistics and synoptic classification

During the cool season, the Alta Ski Patrol records twice-daily 12-h measurements of snow and LPE at 0400 LST and 1600 LST at its Alta-Collins observing site (2945 m MSL; hereafter Collins), approximately 1.7 km south and 271 m higher than the Alta MRR (Wasserstein and Steenburgh 2023, 2025). To focus on heavy precipitation characteristics, we identify 75th-percentile 12-h snow (≥15.2 cm) or LPE (≥14.0 mm) periods at Collins, which we define as an "event" in the rest of this paper. These 75th-percentile thresholds are based on the long-term climatology of WS24. Table S1 in the supplemental material lists the dates of each event over the two-cool-season period. In addition to the 75th-percentile events, our analysis examines combined seasonal data for all periods during which MRR data was available at both sites (Table 1). Out of the potential 670 12-h periods over the two-cool-season period, our seasonal analysis consists of 564 full-coverage periods with available MRR data at Alta and Highland.

We classified the 75th-percentile events using the methods outlined in WS24. To summarize, we used the European Centre for Medium-Range Weather Forecasts Reanalysis v5 (ERA5; Hersbach et al. 2020) to manually classify the events into eight synoptic classifications but focus on three: southerly and southwesterly IVT (S/SWIVT), baroclinic troughs or cold fronts (Frontal), and northwesterly post-frontal events (NW Postfrontal). The S/SWIVT events featured elevated IVT, typically associated with a landfalling atmospheric river, extending toward the central Wasatch from the south or southwest with the local 700-hPa flow between 157.5° and 247.5°. Frontal events featured the passage of a cold front or baroclinic trough and associated precipitation band, the latter identified with operational radar imagery. The NW Postfrontal events featured northwesterly 700-hPa flow behind a cold front or trough with the central Wasatch experiencing cold advection. The S/SWIVT, Frontal, and NW Postfrontal synoptic classifications are the most common climatologically (WS24) and other classifications occurred infrequently during the study period. These three classifications represent the progression of an "ideal" frontal system across the region, although real-world events often do not conform to such a progression. This paper focuses primarily on bulk statistical analyses of events in these synoptic classifications, which risks concealing the variability across multiple events. Examination of MRR data from each event (not shown) suggests that unique characteristic features of each synoptic classification consistently appear in each event and the bulk statistics are generally representative of these unique features.

3. Results

a. Seasonal snowfall and synoptic classifications

The 2022/2023 and 2023/24 cool seasons were exceptionally snowy at Alta, with the former setting the seasonal record for snow and LPE at 2293.6 cm and 1778.8 mm, respectively, and the latter receiving 1614.2 cm and 1493.5 mm of snow and LPE, compared to the climatological means of 1340.4 cm and 1116.9 mm (Figs. 3a-d; WS24). Storms during the 2022/23 season were often colder, yielding a mean snow-to-liquid ratio (SLR) of 15.0, whereas the 2023/24 season featured warmer storms and a mean SLR of 11.2. During the two seasons, there were 114 12-h events that met the 75th-percentile thresholds for either snow or

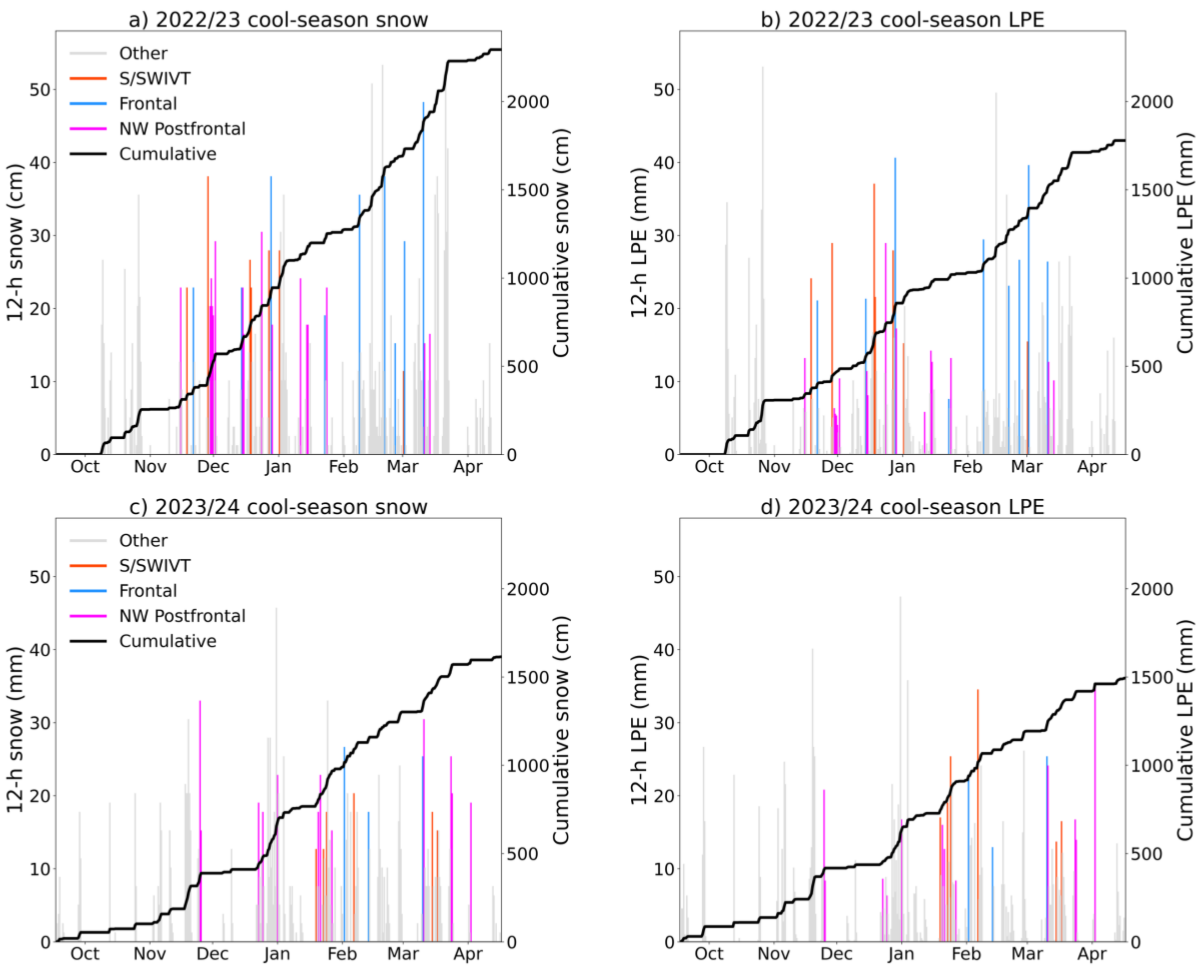

Fig. 3. Bar chart and cumulative time series of manually measured 12-h accumulated snow at Collins snow for (a) 2022/23 and (c) 2023/24. For events during which the MRR recorded data, individual bars are colored based on synoptic classification. (b, d) As in (a) and (c) but for LPE.

LPE. Of those periods, 105 (92.1%) met the snow threshold, 79 (69.3%) met the LPE threshold, and 68 (59.7%) met both thresholds. Based on the long-term climatology of WS24, the mean number of snow and LPE events each cool season is 26 and 23, respectively. Indicative of the snowy nature of the two seasons used in this study, during the 2022/23 cool season, there were 60 and 43 snow and LPE events, respectively, and in the 2023/24 cool season, there were 45 and 36 snow and LPE events, respectively.

We classified 17 (14.9% of all events) events as S/SWIVT, 13 of which had full MRR data coverage at Alta and Highland; these events typically featured moderate snowfall, high LPE, and SLRs much lower than the climatological mean of 13.8 (Table 2; WS24). These events produced 383.5 cm of snow (9.8% of all snow) over the two-cool-season period. 12 of 17 (14.9% of all events) Frontal events were fully sampled by the MRRs, and these had the highest mean snow and LPE of the three classifications and a relatively low mean SLR of 12.6. The 17 Frontal events resulted in 458.5 cm of snow (11.7% of all snow). There were 38 (33.3% of all events) NW Postfrontal events which totaled 870 cm of snow (22.3% of all snow), 28 of which were fully sampled by both MRRs. These events had low mean LPE, but produced notable low-density snow, with mean SLR of 20.5.

Synoptic classification	**Number of Events**	**Mean snow (cm)**	**Mean LPE (mm)**	**Mean SLR**
S/SWIVT	13	21.1	22.8	9.6
Frontal	12	28.3	24.8	12.6
NW Postfrontal	28	21.3	13.1	20.5

Table 2. Statistics for synoptic classifications of events fully sampled by the MRR at Alta and Highland.

Prior work often conceptualizes the evolution of orographic storms based on the passage of a frontal or baroclinic trough including a stable pre-trough stage, frontal stage, and unstable postfrontal stage (Hobbs 1975; Marwitz 1980; Long et al. 1990). Although not all storms follow these stages (e.g., Steenburgh 2003), our synoptic classification generally represents an idealized progression from S/SWIVT to Frontal to NW Postfrontal. S/SWIVT events in northern Utah feature elevated IVT, broad southerly to southwesterly flow, and 700-hPa temperatures near -4°C (Fig. 4a). Frontal events experience a 700-hPa wind shift from southwesterly to northwesterly, with cold advection reducing 700-hPa temperatures as the upper-level trough progresses east (Fig. 4b). The post-cold-frontal environment features low IVT, light, northwesterly 700-hPa winds, and 700-hPa temperatures below -10 °C (Fig. 4c).

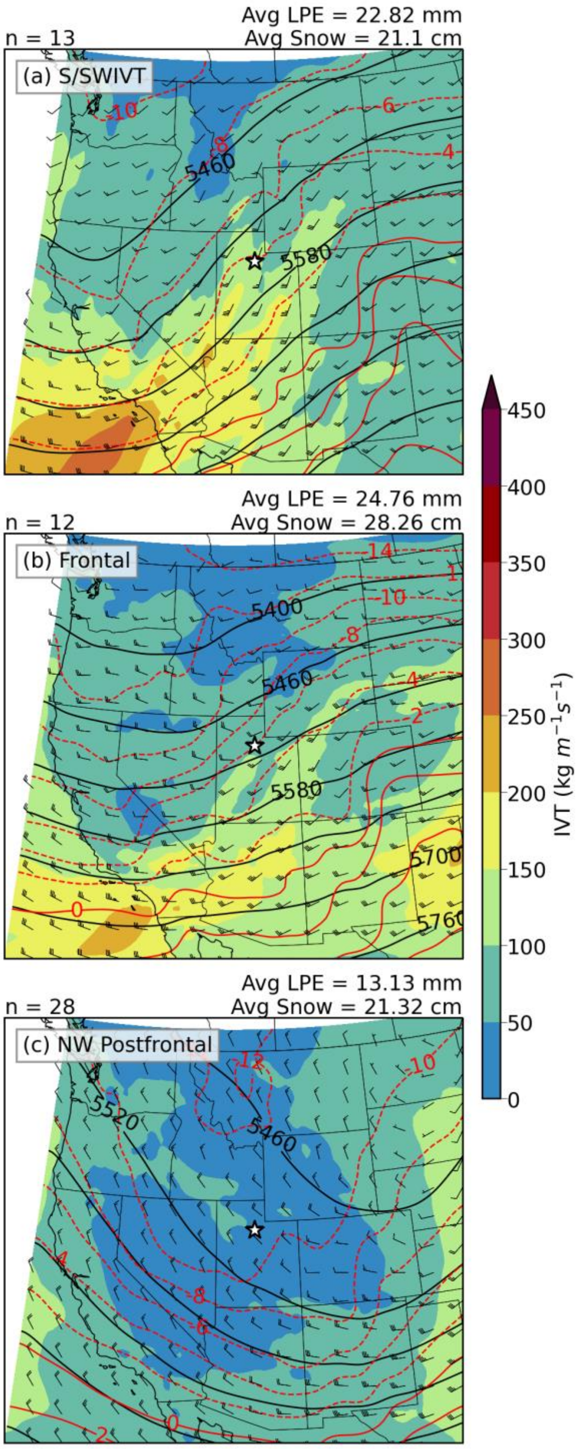

Fig. 4. Composites at the event midpoint (hour 6) of IVT (kg m^{-1} s^{-1}; color–fill scale at bottom), 500-hPa geopotential height (m; black contours), 700-hPa temperature (°C; red contours), and 700-hPa wind (barbs; full barb = 5 m s^{-1}) for (a) S/SWIVT events, (b) Frontal events, and (c) NW Postfrontal events with full MRR coverage. The number of events is annotated at the top left. Average LPE and snow are annotated at the top right. The star indicates the location of the study area.

b. Example events

We selected three representative events to illustrate this conceptual trough passage, introduce the figures used in this paper, and summarize MRR precipitation characteristics of each phase (see Table 3 for the events). The S/SWIVT event featured a deep precipitation system with radar echoes reaching over 6000 m MSL at Alta and Highland (Fig. 5a,b). At Highland, a bright band with Z_e reaching ~30 dBZ$_e$ persisted ~2000–2300 m MSL, indicative of a melting layer below Alta's elevation (Fig. 5b). Above the bright band and below ~3000 m MSL, reflectivity *decreased* toward the ground over Highland prior to ~00:30 UTC 10 January, suggestive of sublimation within a dry sub-cloud layer. Median Z_e at Alta maximized at ~3200 m MSL below which it decreased slightly to the surface (Fig. 5c). At Highland, the median reflectivity similarly maximized ~3200 m MSL, below which the median and quartiles were strongly influenced by the bright band which increased Z_e at ~2000 m MSL due to melting (Fig. 5d). At both sites, the median VRG was near zero but exhibited considerable variability (Fig. 6a). The presence of the bright band, however, limited the utility of the VRG diagnostic during this S/SWIVT event since it frequently resulted in a non-linear low-level profile of Z_e with height.

The Frontal event was not as deep as the S/SWIVT event but echoes still reached ~5500 m MSL above both radars (Figs. 5e,f). At Alta, the median Z_e increased with decreasing height to ~4000 m MSL below which it was nearly constant to the surface (Fig. 5e). The interquartile range (IQR) of Z_e also decreased near the surface, reflecting a narrow Z_e distribution with a pronounced mode ~18 dBZ$_e$, consistent with persistent and steady precipitation. At Highland, the bright band was evident until ~00:30 UTC 22 February after which snow fell to the surface in the wake of the front (Fig. 5f). Although the median Z_e increased with decreasing height to ~3250 m MSL, it decreased weakly below this level toward the ground and the IQR increased, consistent with more variable precipitation (Fig. 5h). At both sites, the VRG was near zero, but exhibited less variability than during the S/SWIVT event (cf. Figs. 6a,b). Some skewness to positive values up to ~8 dBZ$_e$ km^{-1} at Highland reflects a period with apparent low-level precipitation losses late in the event (Figs. 5f,6b).

The NW Postfrontal event featured persistent, shallow, low-density orographic snowfall at Alta, with echo top heights <3600 m MSL (1000 m AGL; Fig. 5i). Modal Z_e increased from ~0 to ~12 dBZ$_e$ with decreasing height in the lowest 900 m (Fig. 5k). The IQR of Z_e was small at all levels, with a narrow Z_e distribution and a mode of ~12 dBZ$_e$ at the surface, consistent with persistent snowfall (Fig. 5k). Nearly all profiles featured a negative VRG, with a median of -15 dBZ_e km^{-1} indicating substantial low-level snow growth (Fig 6c). Precipitation at Highland was also shallow with echo tops <3400 m MSL (Fig. 5j). Median Z_e decreased with height to ~2500 m MSL but decreased weakly below this height toward the surface where the IQR was larger and shifted to lower values compared to Alta, consistent with less persistent and intense snowfall (Fig. 5l). The VRG median near zero indicates that low-level precipitation growth was not as common at Highland, and the positive values indicate that there were periods of precipitation loss due to presumed sublimation or evaporation (Fig. 6c).

Synoptic classification	**Start Time**	**End Time**	**Snow (cm)**	**LPE (mm)**
S/SWIVT	2300 UTC 09 Jan 2023	1100 UTC 10 Jan 2023	27.9	27.9
Frontal	2300 UTC 21 Feb 2023	1100 UTC 22 Feb 2023	35.6	29.5
NW Postfrontal	2300 UTC 13 Dec 2022	1100 UTC 14 Dec 2022	20.3	5.3

Table 3. The three representative examples in a trough conceptualization.

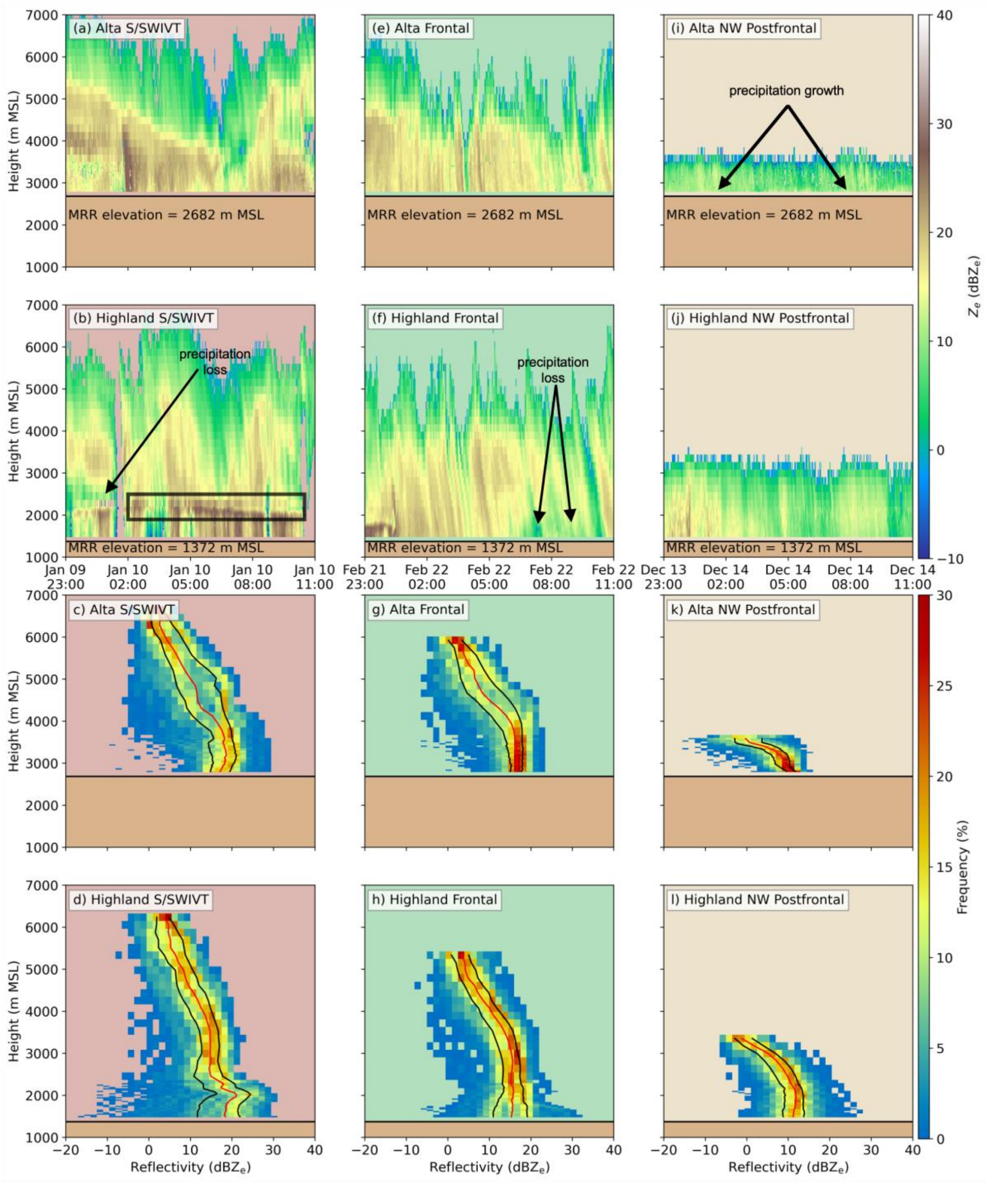

Fig. 5. Time height section of MRR 30-m and 180-m range gate equivalent reflectivity (dBZ$_e$; color-fill scale at right) for (a) Alta and (b) Highland and CFADs of Z_e (%; scale at right) for (c) Alta and (d) Highland during the S/SWIVT event from 2300 UTC 09 January 2023 to 1100 UTC 10 January 2023. The black box in (d) indicates the location of the radar bright band. The CFADs have bin widths of 1.5 dBZ$_e$. The 25th, 50th, and 75th percentiles on the CFADs are indicated by the black, red, and black lines, respectively, and the dark brown shading indicates the ground level. (e)-(h) As in (a)-(d) but for the Frontal event from 2300 UTC 21 February 2023 to 1100 UTC 22 February 2023. (e)-(h) As in (i)-(l) but for the NW Postfrontal event from 2300 UTC 13 December 2022 to 1100 UTC 14 December 2022.

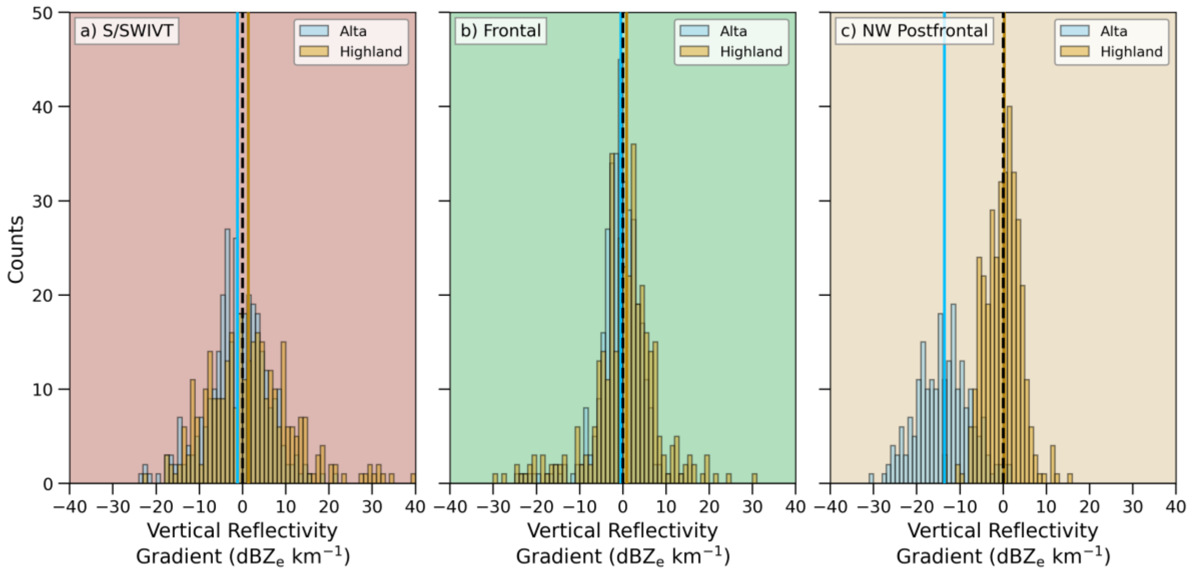

Fig. 6. Histograms of vertical reflectivity gradient for Alta (blue) and Highland (orange) for (a) the S/SWIVT event from 2300 UTC 09 January 2023 to 1100 UTC 10 January 2023, (b) the Frontal event from 2300 UTC 21 February 2023 to 1100 UTC 22 February 2023, and (c) the NW Postfrontal event from 2300 UTC 13 December 2022 to 1100 UTC 14 December 2022. The solid blue and orange vertical lines indicate median values, and the black dashed line indicates 0 dBZ$_e$ km^{-1}.

c. Seasonal precipitation frequency statistics

At Alta, the frequency of Z_e ≥5 dBZₑ during the 2022/23 and 2023/24 cool seasons increases with decreasing height and maximizes in the lowest useable range gate (Fig. 7). Increasing frequency of Z_e ≥5 dBZₑ with decreasing height does not necessarily imply greater precipitation intensity, but it does highlight the high *frequency* of low-level radar echoes at Alta, where strong low-level snow growth within a shallow layer can occur. The low-level frequency of Z_e ≥5 dBZₑ of ~25% demonstrates the persistent nature of snowfall at Alta. At Highland, the maximum frequency of Z_e ≥5 dBZₑ occurs at a similar altitude (MSL) to Alta but is roughly half of the magnitude (Fig. 7). Below ~2600 m MSL, the frequency of Z_e ≥5 dBZₑ *decreases* with decreasing elevation, which is likely indicative of sublimation and evaporation in dry sub-cloud layers that are sometimes resident at low levels in this continental mountain environment (e.g., Schultz and Trapp 2003; Steenburgh 2003). Comparison of the frequency of Z_e ≥5 dBZₑ echoes at the surface suggests an increase by a factor of 2.5 in the frequency of measurable precipitation from Highland (~10%) to Alta (~25%).

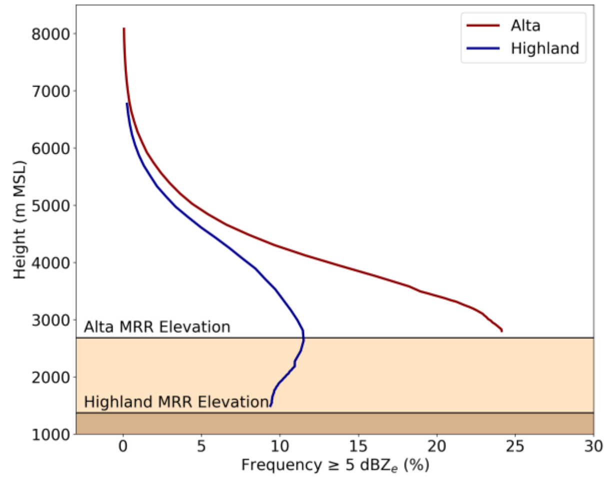

Fig. 7. Frequency of equivalent reflectivity ≥ 5 dBZ_e at Alta and Highland during all periods with sufficient MRR data at both sites during the 2022/23 and 2023/24 cool seasons. The brown shading indicates the ground level.

d. S/SWIVT statistics

At Alta, S/SWIVT events were the warmest and had the lowest SLRs of the three synoptic classifications (Table 2; Fig. 4a). The CFAD demonstrates a median and modal Z_e increase with decreasing height down to ~1000 m AGL below which they remain nearly constant (Fig. 8a). At the lowest usable range gate, 80% of all observations featured $Z_e \geq 5$ dBZ_e, indicative of persistent mountain precipitation (Fig. 9a). Median low-level VRG was near zero, which suggests that some S/SWIVT events experience low-level snow loss and others exhibit snow growth (Fig. 10a). Echo top height frequency exhibited bimodality with modes at 4572 m MSL (1890 m AGL) and 6192 m MSL (3510 m AGL; Figs. 11a,b). The cause of this bimodality is unclear, but one possibility is the occasional presence of upper-level generating cells that produce ice crystals aloft and seed low-level feeder clouds. Another is the invigoration of convection during orographic uplift, promoting growth of a deeper cloud. To definitively determine which of these mechanisms is responsible for the bimodality, higher resolution radar data that can resolve seeder and feeder clouds or convective cells embedded within the broader cloud field would be necessary.

At Highland, the median and modal Z_e tends to increase with decreasing height down to 1000 m AGL; below that, the IQR widens, with the Z_e corresponding with the 25^{th}-percentile frequency decreasing and the 75^{th}-percentile frequency increasing (Figs. 8b,c). This implies that there can be low-level precipitation growth or loss during S/SWIVT events, which is further apparent in the VRG, which has a median value near 0 dBZ_e km^{-1}, but a wider distribution than at Alta (Fig. 10a). We note, however, that the presence of melting can impact Z_e and limit the utility of VRG during S/SWIVT events. Highland's frequency of Z_e ≥5 dBZ_e was <40% in the lowest ~800 m AGL and there was a high frequency of periods with no radar echoes recorded at the top or bottom of the layer depth used to calculate VRG, consistent with Highland's lack of precipitation during precipitating periods at Alta (Figs. 9a;10b). The echo top height distribution at Highland during S/SWIVT events was modal, with a median of 5242 m MSL (3870 m AGL; Figs. 11a,b).

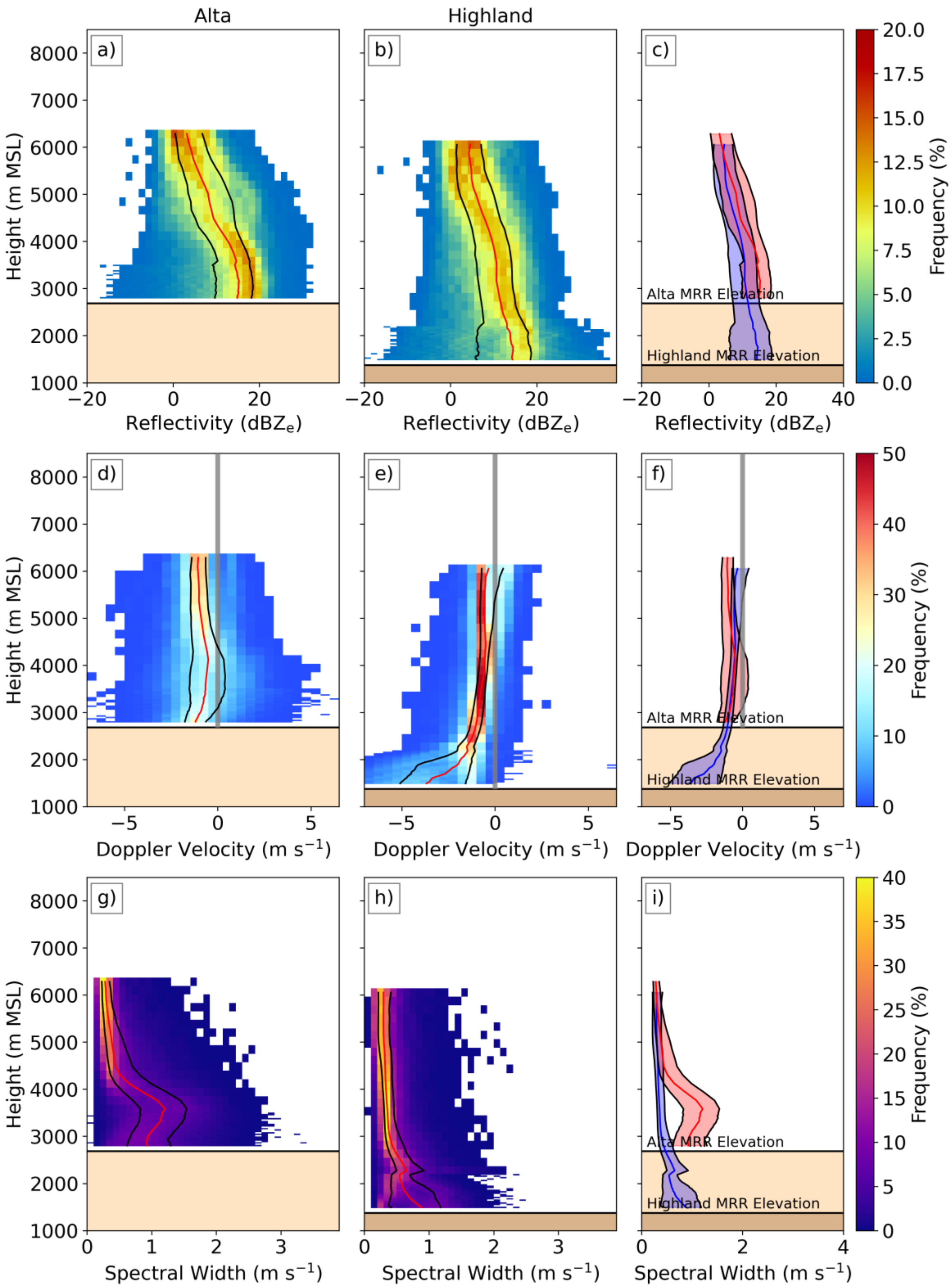

Fig. 8. CFADs of Z_e for S/SWIVT events at (a) Alta and (b) Highland. The 25th, 50th, and 75th percentiles are indicated by the black, red, and black lines, respectively. The brown shading indicates the ground level. (c) CFAD interquartile range for Alta (red) and Highland (blue). (d-f) As in (a-c), but for Doppler radial velocity. The grey line indicates 0 m s^{-1}. (g-i) As in (a-c), but for spectral width. The 2D histograms have bin widths of 1.5 dBZ$_e$, 0.5 m s^{-1}, and 0.1 m s^{-1} for Z_e, V_r, and SW, respectively and bin heights of 30 m up to 810 m AGL and 180 m above 810 m AGL.

409

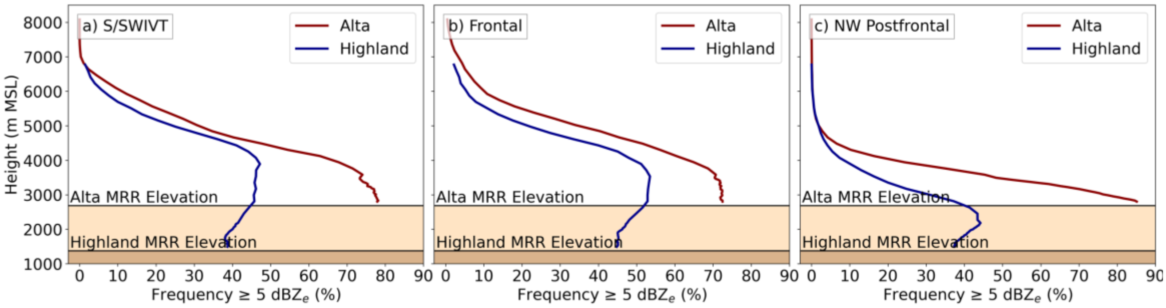

Fig. 9. As in Fig. 7 but for (a) S/SWIVT, (b) Frontal, and (c) NW Postfrontal events.

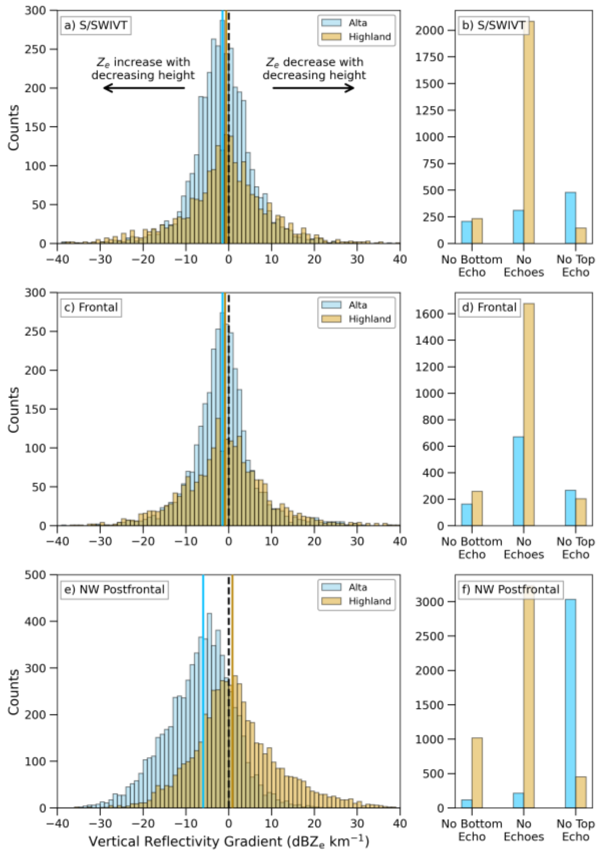

Fig. 10. Histograms of vertical reflectivity gradient for Alta (blue) and Highland (orange) for (a) S/SWIVT, (c) Frontal, and (e) NW Postfrontal events. The solid blue and orange vertical lines indicate median values, and the grey vertical lines indicate 0 dBZ_e km^{-1}. Shown at right are bar charts of the number of occurrences of no echoes at the bottom of the layer depth, the top and bottom of the layer depth, and at the top of the layer depth for (b) S/SWIVT, (d) Frontal, and (f) NW Postfrontal events.

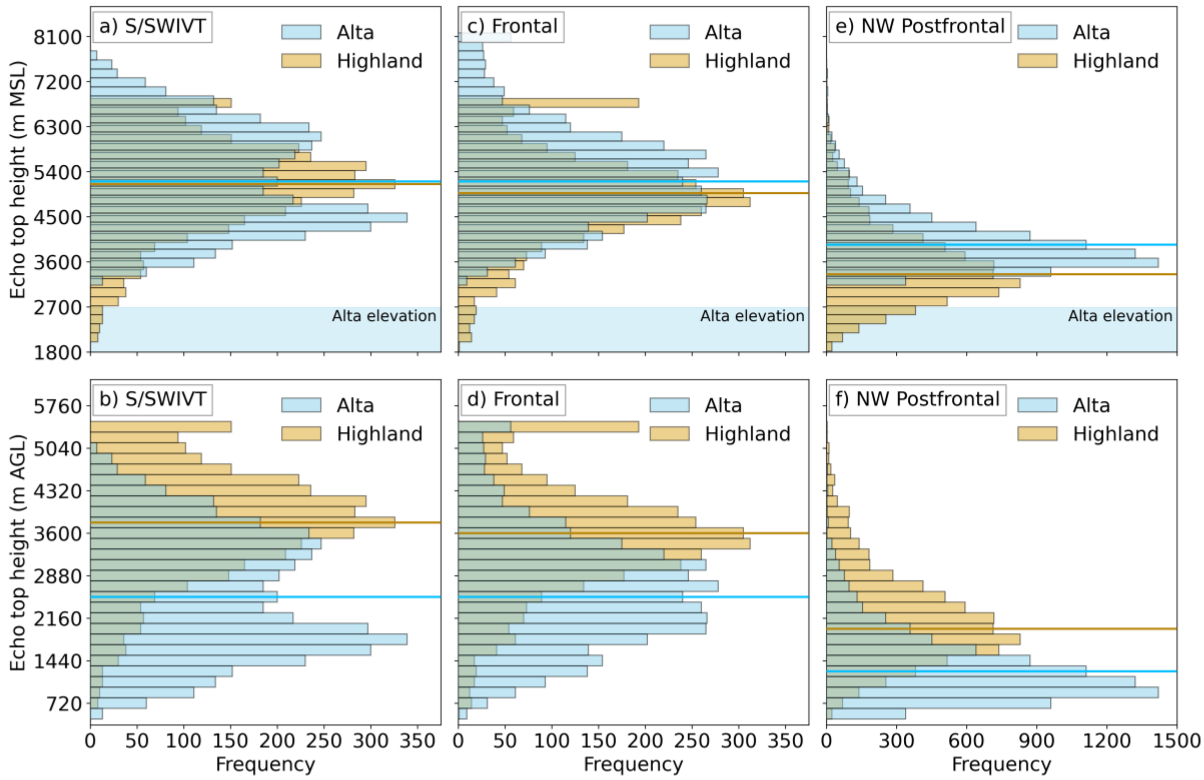

Fig. 11. Histograms of echo top (-10 dBZe) height frequency above sea level for Alta (blue) and Highland (orange) for (a) S/SWIVT, (c) Frontal, and (e) NW Postfrontal events and above ground level for (b), S/SWIVT, (d) Frontal, and (f) NW Postfrontal events. Bin width is 180 m. The thick horizontal lines indicate median values, and the blue shading indicates the elevation of the Alta MRR.

Doppler velocity reflects the combination of air vertical velocity and hydrometeor fall speed, with the latter typically dominating. V_r is sometimes defined to be negative toward the radar (e.g., Minder et al. 2015; Ackermann et al. 2021), whereas fall speed is typically expressed as a positive quantity and some authors have defined V_r to be positive toward the ground (Stark et al. 2013; Pettersen et al. 2020). In our analysis, negative V_r indicates downward hydrometeor vertical motions towards the MRR, whereas positive V_r implies upward vertical motions. Empirical studies have suggested typical fall speeds of ~0.5-1.5 m s^{-1} for individual dendrites and aggregates of dendrites, 1-2.5 m s^{-1} for graupel, and 3-7 m s^{-1} for rain assuming the absence of upward air motions (Locatelli and Hobbs 1974; Bringi et al. 2018; Das et al. 2020). At Alta, the IQR of V_r ranges from roughly -0.5 to -2 m s^{-1} during S/SWIVT events for most of the atmosphere, characteristic of high-elevation snowfall (Figs. 8d,f). Between ~3500 m MSL and ~4250 m MSL, the 75^{th}-percentile V_r is weakly positive, which we suggest is due to updrafts near mountain crest level and may be associated with riming and aggregation, leading to increasing Z_e with decreasing height through that layer

(Figs. 8d,f). At Highland, upward V_r between ~3500 m MSL and ~4250 m MSL is much less common than at Alta, and as height decreases below 3000 m MSL, V_r at Highland becomes increasingly negative as hydrometeors fall to the surface and the 25th-percentile frequency decreases to <-5 m s^{-1}, consistent with the occasional presence of valley rain during warmer S/SWIVT events (Figs. 8e,f). The presence of rain at Highland is also evident in the PARSIVEL data, which features a bimodal distribution (Fig. 12a). During S/SWIVT events at Highland, hydrometeors most frequently fall as rain with diameter ≤4 mm and fall velocity ≥4 m s^{-1}, while graupel and dendrites comprise the secondary mode in colder events. The difference in precipitation fall speed characteristics between the two sites reflects the tendency for the melting layer to be situated between the elevation of the two locations during S/SWIVT events (e.g., Figs. 5b;8e).

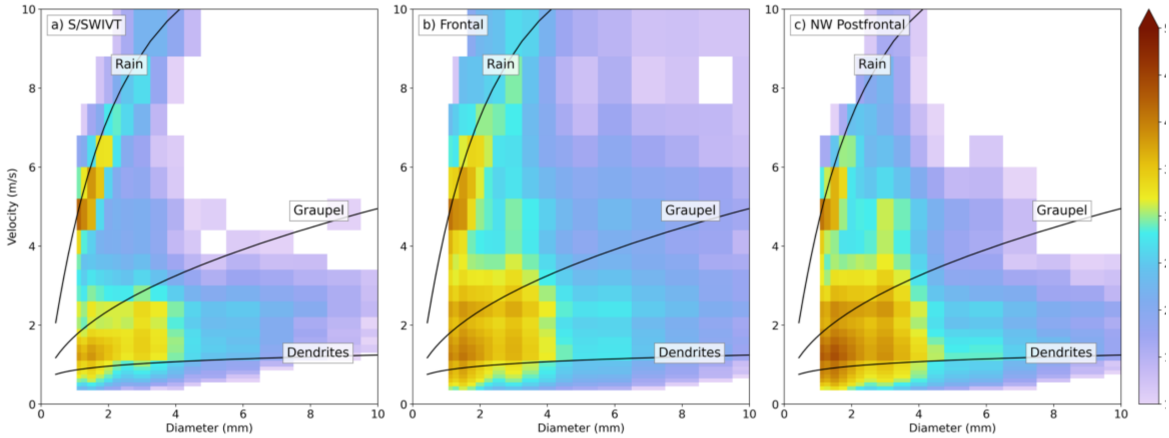

Fig. 12. Summed PARSIVEL matrix for a) S/SWIVT, b) Frontal, and c) NW Postfrontal events at Highland. Bins are based on the bins recorded by the PARSIVEL. Empirical fall speed relationships from Locatelli and Hobbs (1974) and Berry and Pranger (1974) are overlaid and labeled for hydrometeor type.

During S/SWIVT events, modal *SW* frequency at Alta maximizes at ~1000 m AGL (Figs. 8g,i). We hypothesize that this is due to wind shear within range gates, differential hydrometeor fall velocity or size, or boundary layer turbulence that is strongest on the ridgelines above the Alta MRR (Houze and Medina 2005; Geerts et al. 2011; Majewski et al. 2023). At Highland, median and 75th-percentile *SW* frequency are <0.4 m s^{-1} down to ~2700 m MSL and increase to the surface (Figs. 8h,i). We suggest that air turbulence at upper levels is weaker than at Alta, but the low-level increase in *SW* frequency could be associated with boundary layer turbulence or an increase in differential hydrometeor fall velocity or size due to the transition to rain during some events at Highland.

e. Frontal statistics

At Alta, echo top height during Frontal events is unimodal and relatively high, with the greatest frequency ~5400 m MSL (2718 m AGL; Figs. 11c,d). The modal CFAD reflectivity at Alta increases slightly with decreasing height in the lowest 1 km AGL (Fig. 13a). The tendency for small low-level Z_e increases is evident through VRG, which has a median near -2 dBZ$_e$ km^{-1} at Alta (Fig. 10c). Frequency of Z_e ≥5 dBZ$_e$ at Alta during Frontal events increases with decreasing height and maximizes at ~75% at the lowest usable range gate (Fig. 9b). Compared to S/SWIVT events, the near-ground frequency of Z_e ≥5 dBZ at Alta is lower, suggesting that precipitation is less persistent (c.f. Figs. 9a,b).

At Highland, Frontal events were deep, with the median echo top height frequency near 4800 m MSL (3428 m AGL) and a spike in echo top frequency at the highest detectable range gate (Figs. 11c,d). Median reflectivity increases with decreasing height down to 4000 m MSL below which it remains relatively consistent (Fig. 13b). In the lowest ~1000 m AGL at Highland, the IQR widens, with the 75th-percentile Z_e frequency increasing and the 25th percentile decreasing (Figs. 13b,c). We suggest that this is due to a transition from snow to rain below the melting layer increasing reflectivity during events with rain, and sub-cloud evaporation or sublimation lowering reflectivity in events with low-level dry layers. The distribution of VRG at Highland is nearly Gaussian and centered at 0 dBZ$_e$ km^{-1}, and there is more variability than at Alta (Fig. 10c). Frontal events at Highland often feature no echoes at the top and bottom of the layer depth, consistent with nonprecipitating periods (Fig. 10d). The profile of frequency of Z_e ≥5 dBZ$_e$ at Highland is nearly identical to that for S/SWIVT events, but frequencies are *higher* for almost all elevations, in contrast to Alta, where they are *lower* (Figs. 9a,b). This implies a smaller mountain-valley precipitation frequency gradient during Frontal events compared to S/SWIVT events.

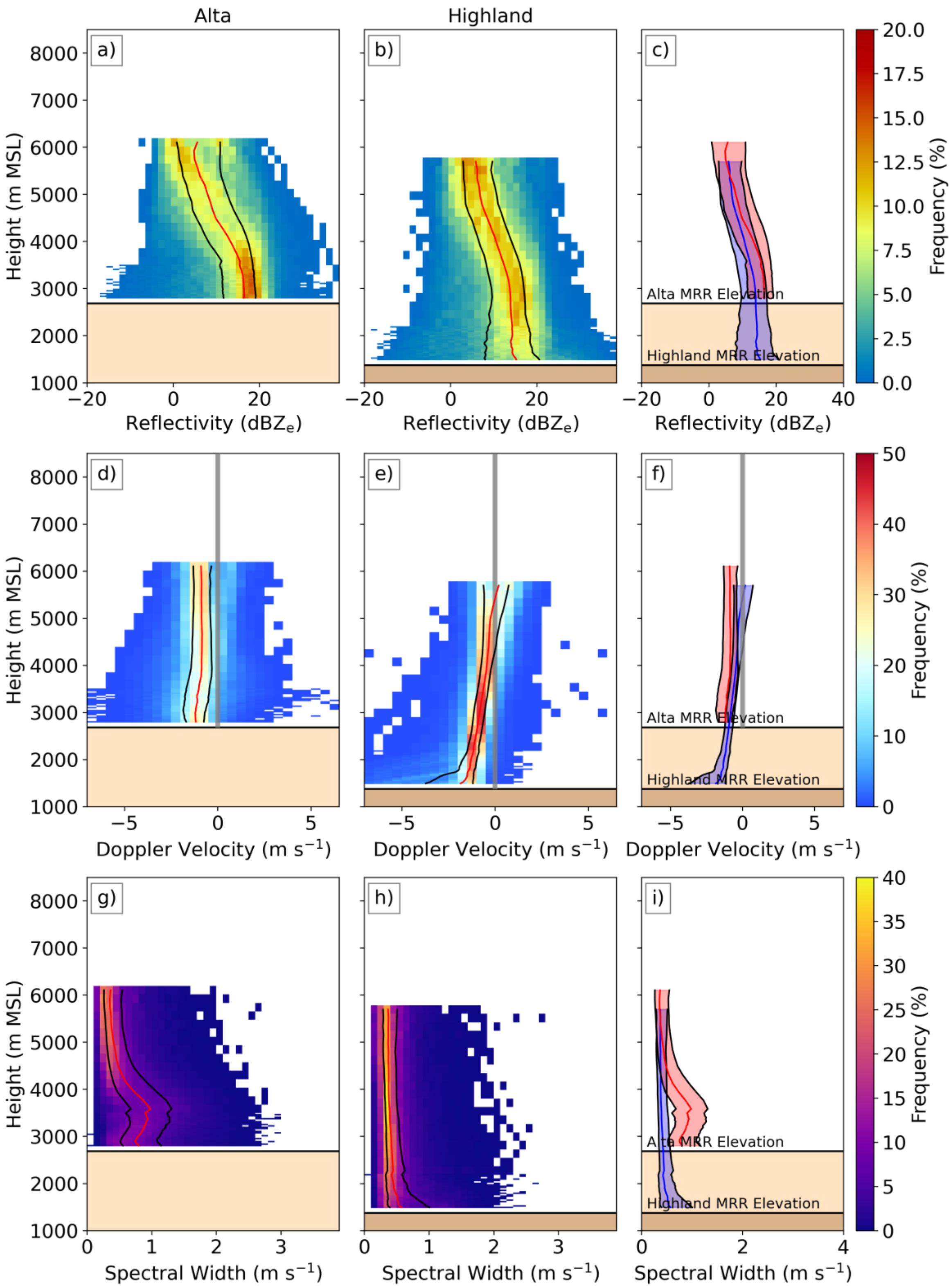

Fig. 13. As in Fig. 8 but for Frontal events.

472

At Alta, modal V_r is consistently between -0.5 and -2.0 m s^{-1} throughout the atmosphere with little variation (as evidenced by the small IQR), indicative of snow or graupel, which have typical terminal fall speeds between 0.5 and 2.5 m s^{-1} (Figs. 13d,f). At Highland, modal V_r is between 0 and -2.0 m s^{-1} throughout the atmosphere and decreases slightly with decreasing height (Fig. 13e). The rapid decrease in the 25th-percentile profile of V_r from ~-2.5 m s^{-1} to ~-4 m s^{-1} in the lowest 500 m AGL reflects a low-level transition to rain in some Frontal events (Fig. 13e). PARSIVEL data at Highland show a high frequency of precipitation with fall speeds ≥2.5 m s^{-1} and diameter ≤3.5 mm, closely following the rain empirical size-fall speed relationship (Fig. 12b). However, compared to S/SWIVT events, there is also a greater frequency of particles with larger diameters, characteristic of graupel or snow (c.f. Figs. 12a,b).

At Alta, the SW CFAD during Frontal events is similar to S/SWIVT events, with median frequency tending to maximize near crest level at around 3600 m MSL, though magnitudes are slightly lower (c.f. Figs. 8g;13g). We hypothesize that this pattern is due to orographic boundary layer turbulence or wind shear at the high elevation site (Houze and Medina 2005; Geerts et al. 2011; Majewski et al. 2023). Above ~1000 m AGL, median SW frequency at Highland is most frequently <0.4 m s^{-1}, although there is a slight increase at the lowest levels, especially in the 75th percentile (Figs. 13h,i). We suggest that the low-level increase in 75th-percentile SW frequency is associated with boundary layer turbulence or an increase in differential hydrometeor size or fall velocity due to a transition to rain in some Frontal events.

f. NW Postfrontal statistics

In contrast to S/SWIVT and Frontal events, NW Postfrontal events are shallow and feature low-density snow (Table 2). At Alta, Z_e frequency increases considerably with decreasing height, with the 25th-, 50th-, and 75th- percentile frequencies increasing by ~10 dBZ$_e$ in the lowest 1500 m (Figs. 14a,c). This low-level Z_e increase is further exemplified by the VRG, which has a median of approximately -6 dBZ$_e$ km^{-1} at Alta, providing evidence of strong low-level snow growth (Fig. 10e). Additionally, there was a high frequency of periods that featured no radar echoes at the top of the layer depth but did contain echoes at the bottom, indicative of low-level snow growth (Fig. 10f). Echo top heights were most frequently ~3600 m MSL (918 m AGL) at Alta, a level *much* lower than S/SWIVT and Frontal events (Fig. 11). Just above the elevation of the Alta MRR, frequency of Z_e ≥5 dBZ$_e$ exceeds 85%, demonstrating the persistence of these NW Postfrontal systems, where precipitation often lingers for long durations after frontal passage (Fig. 9c). Additionally, frequency of Z_e ≥5 dBZₑ increases from ~5% to over 85% in the lowest 2000 m, compared to much smaller increases in S/SWIVT and Frontal events (Fig. 9).

Echo top height at Highland during NW Postfrontal events is similarly low, with the median near 3000 m MSL (1628 m AGL; Fig. 11f). Compared to maxima near 4000 m MSL for S/SWIVT and Frontal events, NW Postfrontal events at Highland had a lower elevation of maximum frequency of Z_e ≥5 dBZₑ, with values maximizing at around 45% at 2500 m MSL, before decreasing to below 40% at the surface (Fig. 9c). This surface frequency is less than half of Alta's frequency during NW Postfrontal events, suggesting that precipitation is more persistent at the mountain site, likely due to orographic effects (Fig. 9c). In contrast to S/SWIVT and Frontal events, the VRG at Highland during NW Postfrontal events has a positive median, consistent with low-level precipitation loss (Fig. 10e). The high frequency of periods with no echoes at the bottom of the layer depth reflects a high frequency of nonprecipitating periods (Fig. 10f).

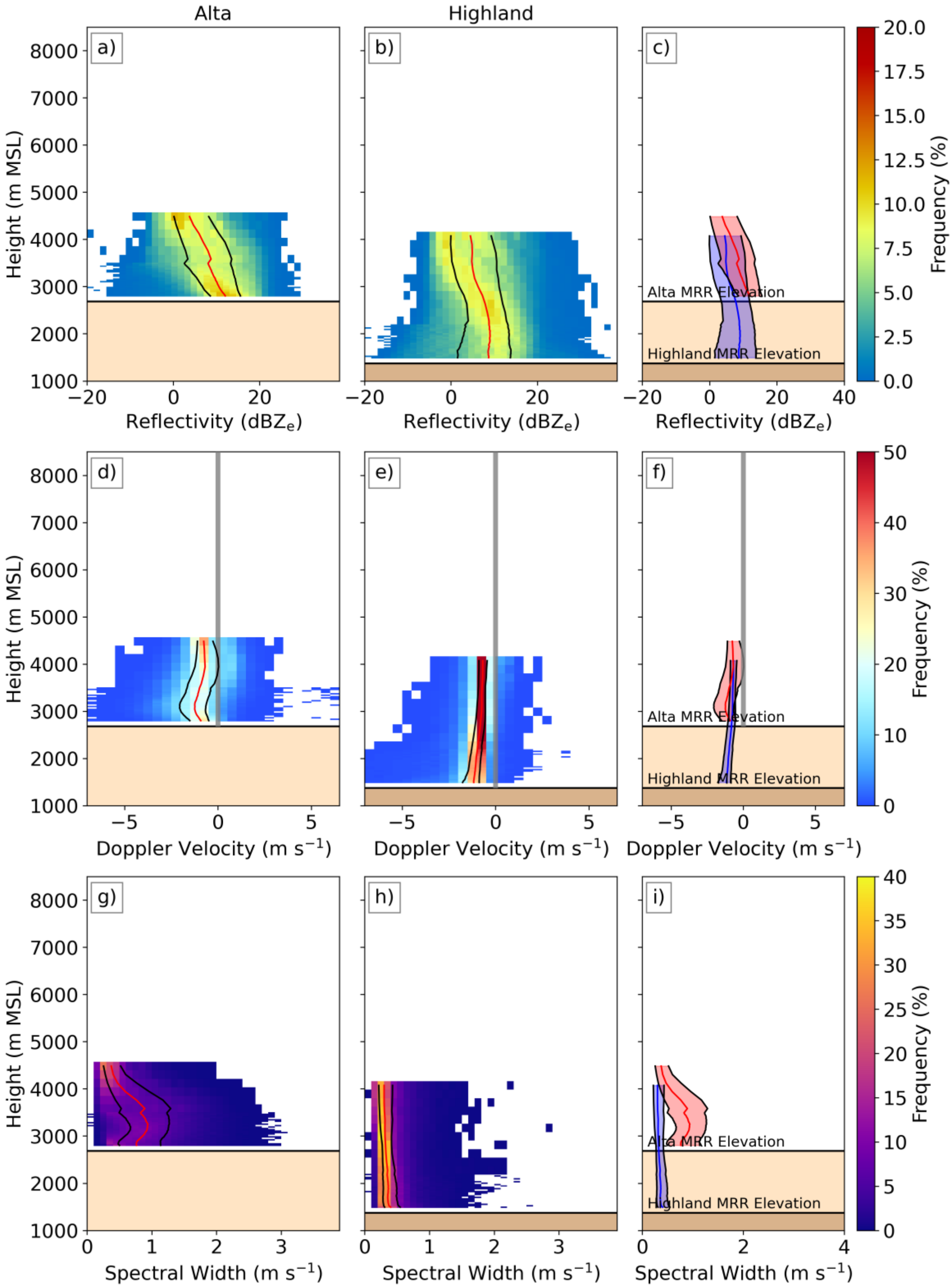

Fig. 14. As in Fig. 8 but for NW Postfrontal events.

519

At Alta, V_r frequency during NW Postfrontal events has limited variability, with the IQR featuring a tight clustering between -0.5 and -2 m s^{-1} (Figs. 14d,f). There is a slight decrease in median V_r at roughly 600 m AGL, potentially indicative of low-level snow growth and aggregation increasing fall velocities of hydrometeors at the lowest levels (Figs. 14d,f). The small increase in V_r corresponding with 75th-percentile frequency at 4000 m MSL at Alta could represent updrafts at that elevation (Fig. 14f). At Highland, the IQR of V_r is relatively small at all elevations, with values consistently between -0.5 and -2 m s^{-1} (Figs. 14e,f). Of the three event types, PARSIVEL data show that precipitation at Highland during NW Postfrontal events tends to most frequently have large diameters with fall speed <2 m s^{-1}, although rain still does occur occasionally (Fig. 12c). The greater frequency of solid precipitation reflects the colder, lower SLR nature of NW Postfrontal storms (Fig. 4c; Table 2).

The SW CFAD for Alta features an increase in the median at ~1000 m AGL (Fig. 14g). At Highland, modal SW is ≤0.4 m s^{-1} during NW Postfrontal events, and in contrast to S/SWIVT and Frontal events, there is no low-level increase in the 75th-percentile SW frequency (Fig. 14g). We suggest that the increased SW at Alta compared to Highland contributes to the low-level Z_e increases at Alta, with turbulence serving as a mechanism to enhance snow growth and aggregation at the mountain site (Houze and Medina 2005; Geerts et al. 2011). Additionally, the decrease in V_r at Alta at ~3000 m MSL suggests that graupel could be present at times in NW Postfrontal storms, contributing to an increase in hydrometeor variability and SW (Figs. 14d,g).

4. Conclusions

This study examined the orographic influences on precipitation in the Salt Lake Valley and the adjacent Wasatch, where cool-season snowfall builds a snowpack which provides water resources and supports winter tourism but can cause extreme avalanche danger. Our research focused on the exceptionally snowy 2022/23 and 2023/24 cool seasons, where 2293.6 and 1614.2 cm of snow fell at Alta, respectively. During those seasons, we operated MRRs and PARSIVELs at Alta and Highland High School in the upstream valley to observe precipitation characteristics during winter storms.

Our research focused on 75th percentile snow and LPE events associated with southerly or southwesterly flow with elevated IVT, cold frontal passages, and post-cold-frontal northwesterly flow. Our results indicate that precipitation is more frequent at Alta than at Highland, presumably due to precipitation growth related to orographic processes at Alta and low-level precipitation losses due to sub-cloud sublimation and evaporation at Highland. Frontal and S/SWIVT events are deepest and there is a bimodal echo top height distribution at Alta during S/SWIVT events. The cause of this bimodality is uncertain, but it could be due to the intermittent presence of upper-level seeder clouds that form ice crystals which seed lower-level feeder clouds, or from enhanced convection during orographic uplift, which stimulates deeper cloud growth. A lower vertical reflectivity gradient and median echo top height AGL at Alta compared to Highland indicate stronger low-level precipitation growth at the mountain site, especially during NW Postfrontal events.

MRR data at Alta indicates that precipitation has the lowest V_r values (i.e., most negative V_r indicating higher hydrometeor fall speeds) during S/SWIVT events and the highest V_r values (i.e., weakly negative indicating smaller fall speeds) in NW Postfrontal events. This suggests a progression from heavily rimed snow and graupel in S/SWIVT events to lightly rimed dendrites and aggregates in NW Postfrontal events, although there can be considerable variability in crystal type within synoptic classifications. Prior research in Marquette, Michigan and Hyytiälä, Finland has similarly found that that warmer, high IVT events feature snow particles with higher density and fall speeds compared to low-IVT events (Richter et al. 2025). At upper levels above Highland, V_r is frequently near zero, but below ~1000 m AGL there is an abrupt decrease in V_r (i.e., greater fall speeds) associated with a transition to rain in S/SWIVT events and a slight V_r decrease in NW Postfrontal events which are predominantly snow. Alta has larger mid-level SW than Highland, indicative of greater air turbulence related to gravity wave breaking and wind shear. At low levels in S/SWIVT and Frontal events, median SW at Highland increases, which could be associated with boundary layer turbulence or an increase in differential hydrometeor fall velocity or size due to a transition to rain in some storms.

While precipitation in coastal mountain ranges in western North America is often deep, with high reflectivity far above ground level (Yuter et al. 2011; McMurdie et al. 2018), our analysis reveals that precipitation in the Wasatch, a continental mountain range, can be remarkably shallow, especially in the post-frontal environment. This shallow, near-surface snow growth is also seen in lower-elevation lake-effect regions such as New York's Tug Hill Plateau or Marquette, Michigan (e.g., Minder et al. 2015; Pettersen et al. 2020), although at

Alta, NW Postfrontal events can be orographic, lake-effect, or a combination of the two (e.g., Steenburgh 2003; Alcott and Steenburgh 2013). The Wasatch's terrain complexity and its shallow storms can limit the ability of the local operational weather radar to detect precipitation (Wood et al. 2003). Additionally, given the shallow nature of many storms at Alta, many heavy precipitation periods are likely under sampled by spaceborne radars and precipitation sensors – which often underestimate precipitation at rage gates closest to earth's surface due to the presence of ground clutter and complex terrain – contributing to an inaccurate representation of regional precipitation (Barros and Arulraj 2020; Chavez et al. 2020; Valdivia et al. 2022).

In the Salt Lake Valley, our analysis demonstrates a slight decline in low-level reflectivity toward the ground, which we hypothesize is due to sub-cloud sublimation and evaporation in dry sub-cloud airmasses that are commonly resident at low levels in this continental mountain environment. Such a mechanism, which has been shown to reduce valley precipitation during individual events in the region (Schultz and Trapp 2003; Steenburgh 2003), is commonly neglected or underappreciated in orographic precipitation reviews that typically focus on enhancement processes. Our research suggests that low-level sublimation and evaporation have a non-negligible effect on seasonal profiling radar statistics and may contribute to the precipitation gradient with altitude in northern Utah. Future research should verify this process and test its influence in other global continental mountain environments.

Acknowledgments.

This material is based upon work supported by the National Science Foundation under Grants AGS-1929602 and AGS-2227071. Any opinions, findings, and conclusions or recommendations expressed in this material are those of the authors and do not necessarily reflect the views of the National Science Foundation. We thank Claire Pettersen, two anonymous reviewers, and the editor for scientific input and recommendations that significantly improved this manuscript, Alta Ski Patrol for providing high-quality snow observations, and the University of Utah Center for High Performance Computing for providing computing resources.

Data Availability Statement.

The ERA5 reanalysis data used in this research were obtained from the Copernicus Climate Change Service. We thank the Alta Ski Patrol for providing a high-quality dataset of manual snow and LPE observations which is online and freely available from the University of Utah Research Data Repository for the 1999-2023 and 2023-2024 periods (Wasserstein and Steenburgh 2023, 2025). The MRR data for Alta and Highland during the 2022/23 and 2023/24 cool seasons are openly available online from the University of Utah Research Data Repository (Steenburgh et al. 2025a; Veals et al. 2025). Similarly, the PARSIVEL data for both sites for the 2022/23 and 2023/24 cool seasons are available from the University of Utah Research Data Repository (Steenburgh et al. 2025b,c). The radar postprocessing algorithm code is available at https://github.com/maahn/IMProToo. Code used to analyze data and produce figures is available at https://github.com/mwasserstein/Code_For_Wasserstein_2026.

APPENDIX A

List of Acronyms and Symbols Used in the Text

CFAD = Contoured Frequency by Altitude Diagram

IQR= Interquartile Range

IVT = Integrated Vapor Transport

LPE= Liquid Precipitation Equivalent

MRR = Micro Rain Radar 2

SLR = Snow to Liquid Ratio

$\boldsymbol{SW}$= Spectral Width

$\boldsymbol{V_r}$= Doppler Velocity

VRG= Vertical Reflectivity Gradient

$\boldsymbol{Z_e}$= Equivalent Reflectivity

APPENDIX B

Discontinuity Explanation

Here, we present an explanation for the discontinuity in statistics that occasionally occurs at the transition between 30-m and 180-m range gate resolutions. The MRR experiences *leakage* of a power peak detected in one range gate into adjacent range gates. Specifically, a peak located in the center of range gate n contributes Z_e – 3 dBZ_e to the adjacent range gates n + 1 and n – 1 (G. Peters, Metek, 2025, personal communication).

Analyses of time-height profiles of individual events indicated that the discontinuity occurred more often at Highland and during periods with the melting layer and associated radar bright band located just below the transition. One such event was a S/SWIVT event that occurred during the period 2300 UTC 9 January 2023 through 1100 UTC 10 January 2023 (Fig. A1). At roughly 0800 UTC 10 January, the melting layer and associated radar bright band at Highland were just below the transition between the 30-m and 180-m data at ~730 m AGL (Figs. A1d-f). Thus, this power peak would be detected by a 30-m gate centered at 720 m AGL and spanning from 705 to 735 m AGL. But due to leakage, the detected power is also observed in adjacent range gates centered at n – 1 = 690 and n + 1 = 750 m AGL, so that the feature spans a 90-m layer depth from 675 to 765 m AGL. Similarly, the power peak would be detected by a 180-m range gate centered at 720 m AGL, but leakage would cause the power to be distributed to adjacent gates centered at 540 and 900 m AGL. For plotting purposes, radar power associated with the melting layer would then be visualized from 675 to 765 m AGL for the 30-m range gate data and from 450 to 990 m AGL for the 180-m range gate data. Consequently, the discontinuity in data can be detected for Z_e, V_r, and SW at the transition from the 30-m to 180-m range gate data (Figs. A1d-f).

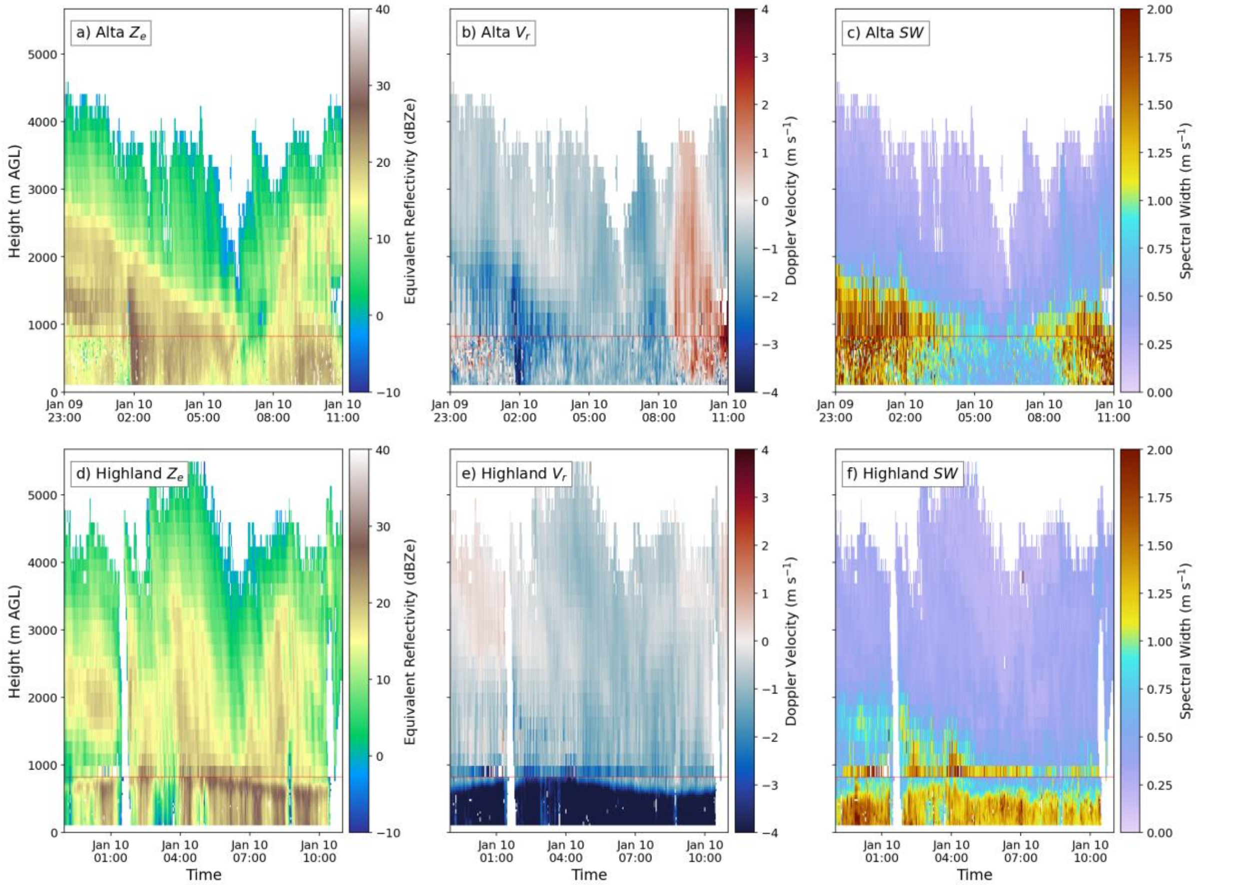

Fig. A1. MRR time-height sections of (a) equivalent reflectivity (dBZ$_e$; scale at right), (b) Doppler velocity (m s^{-1}; scale at right), and (c) spectral width (m s^{-1}; scale at right) for the Alta during the period 2300 UTC 9 January 2023 through 1100 UTC 10 January 2023. The horizontal red line denotes the height of the transition between the 30-m range gate data and the 180-m data. (d-f) As in (a-c) but for Highland.

REFERENCES

Abel, M. R., A. Hall, and R. G. Fovell, 2009: Blocking in Areas of Complex Topography, and Its Influence on Rainfall Distribution. *J. Atmos. Sci.*, **66**, 508–518, https://doi.org/10.1175/2008JAS2689.1.

Ackermann, L., and Coauthors, 2021: Wintertime Precipitation over the Australian Snowy Mountains: Observations from an Intensive Field Campaign 2018. *J. Hydrometeor.*, **22**, 2193–2211, https://doi.org/10.1175/JHM-D-20-0283.1.

Alcott, T. I., and W. J. Steenburgh, 2013: Orographic Influences on a Great Salt Lake–Effect Snowstorm. *Mon. Wea. Rev.*, **141**, 2432–2450, https://doi.org/10.1175/MWR-D-12-00328.1.

Alta Ski Area, 2023: Rolling In the Deep. *Alta Ski Area*. Accessed 22 April 2025, https://www.alta.com/stories/rolling-in-the-deep.

Bardsley, T., A. Wood, M. Hobbins, T. Kirkham, L. Briefer, J. Niermeyer, and S. Burian, 2013: Planning for an Uncertain Future: Climate Change Sensitivity Assessment toward Adaptation Planning for Public Water Supply. *Earth Interact.*, **17**, 1–26, https://doi.org/10.1175/2012EI000501.1.

Barros, A. P., and M. Arulraj, 2020: Remote Sensing of Orographic Precipitation. *Satellite Precipitation Measurement: Volume 2*, V. Levizzani, C. Kidd, D.B. Kirschbaum, C.D. Kummerow, K. Nakamura, and F.J. Turk, Eds, Springer International Publishing, 559–582, https://doi.org/10.1007/978-3-030-35798-6_6.

Battaglia, A., E. Rustemeier, A. Tokay, U. Blahak, and C. Simmer, 2010: PARSIVEL Snow Observations: A Critical Assessment. *J. Atmos. Oceanic Technol.*, **27**, 333–344, https://doi.org/10.1175/2009JTECHA1332.1.

Berry, E. X., and M. R. Pranger, 1974: Equations for Calculating the Terminal Velocities of Water Drops. *J. Appl. Meteor. Climatol.*, **13**, 108–113, https://doi.org/10.1175/1520-0450(1974)013%3C0108:EFCTTV%3E2.0.CO;2.

Bringi, V., M. Thurai, and D. Baumgardner, 2018: Raindrop fall velocities from an optical array probe and 2-D video disdrometer. *Atmos. Meas. Tech.*, **11**, 1377–1384, https://doi.org/10.5194/amt-11-1377-2018.

Chavez, S. P., Y. Silva, and A. P. Barros, 2020: High-Elevation Monsoon Precipitation Processes in the Central Andes of Peru. *J. Geophys. Res. Atmos.*, **125**, e2020JD032947, https://doi.org/10.1029/2020JD032947.

Cox, J. A. W., W. J. Steenburgh, D. E. Kingsmill, J. C. Shafer, B. A. Colle, O. Bousquet, B. F. Smull, and H. Cai, 2005: The Kinematic Structure of a Wasatch Mountain Winter Storm during IPEX IOP3. *Mon. Wea. Rev.*, **133**, 521–542, https://doi.org/10.1175/MWR-2875.1.

Cunningham, J. G., and S. E. Yuter, 2014: Instability Characteristics of Radar-Derived Mesoscale Organization Modes within Cool-Season Precipitation near Portland, Oregon. *Mon. Wea. Rev.*, **142**, 1738–1757, https://doi.org/10.1175/MWR-D-13-00133.1.

Das, S. K., S. Simon, Y. K. Kolte, U. V. M. Krishna, S. M. Deshpande, and A. Hazra, 2020: Investigation of Raindrops Fall Velocity During Different Monsoon Seasons Over the Western Ghats, India. *Earth Space Sci.*, **7**, e2019EA000956, https://doi.org/10.1029/2019EA000956.

Evans, A. N., 2025: Census of Valley and Mountain Profiling Radar Characteristics During Winter Storms Along Utah's Wasatch Front. University of Utah.

Foote, G. B., and P. S. D. Toit, 1969: Terminal Velocity of Raindrops Aloft. *J. Appl. Meteor. Climatol.*, **8**, 249–253, https://doi.org/10.1175/1520-0450(1969)008%3C0249:TVORA%3E2.0.CO;2.

Geerts, B., Q. Miao, and Y. Yang, 2011: Boundary Layer Turbulence and Orographic Precipitation Growth in Cold Clouds: Evidence from Profiling Airborne Radar Data. *J. Atmos. Sci.*, **68**, 2344–2365, https://doi.org/10.1175/JAS-D-10-05009.1.

Hagen, M., A. Häring, S. Kneifel, and K. Schmidt, 2022: Cloud and Precipitation Observed with Radar. *Science at the Environmental Research Station Schneefernerhaus/Zugspitze*, 79–95.

Hardin, N. R., S. E. Yuter, and Katja Friedrich, 2011: Observed vertical structure of snow storms in Steamboat Springs, CO: Orographic enhancement in a high altitude environment. *24th Conf. on Weather and Forecasting*, Seattle, WA, Amer. Meteor. Soc., 108, https://ams.confex.com/ams/91Annual/webprogram/Paper182337.html.

Hersbach, H., and Coauthors, 2020: The ERA5 global reanalysis. *Q. J. R. Meteorol. Soc.*, **146**, 1999–2049, https://doi.org/10.1002/qj.3803.

Hobbs, P. V., 1975: The Nature of Winter Clouds and Precipitation in the Cascade Mountains and their Modification by Artificial Seeding. Part I: Natural Conditions. *J. Appl. Meteor. Climatol.*, **14**, 783–804, https://doi.org/10.1175/1520-0450(1975)014%3C0783:TNOWCA%3E2.0.CO;2.

Houze Jr., R. A., 2012: Orographic effects on precipitating clouds. *Rev. Geophys.*, **50**, 1–47, https://doi.org/10.1029/2011RG000365.

Houze, R. A., and S. Medina, 2005: Turbulence as a Mechanism for Orographic Precipitation Enhancement. *J. Atmos. Sci.*, **62**, 3599–3623, https://doi.org/10.1175/JAS3555.1.

Jag, J., 2023: Avalanche chaos causes Cottonwood Canyon closures, strands thousands. *Salt Lake Tribune*, https://doi.org/www.sltrib.com/sports/2023/04/05/avalanche-chaos-causes-cottonwood/.

Kneifel, S., M. Maahn, G. Peters, and C. Simmer, 2011: Observation of snowfall with a low-power FM-CW K-band radar (Micro Rain Radar). *Meteorol. Atmos. Phys.*, **113**, 75–87, https://doi.org/10.1007/s00703-011-0142-z.

——, and Coauthors, 2022: Multi-year cloud and precipitation statistics observed with remote sensors at the high-altitude Environmental Research Station Schneefernerhaus in the German Alps. *Meteorol. Z.*, 69–86, https://doi.org/10.1127/metz/2021/1099.

Koszuta, M., N. Siler, L. R. Leung, and J. J. Wettstein, 2024: Weakened Orographic Influence on Cool-Season Precipitation in Simulations of Future Warming Over the Western US. *Geophys. Res. Lett.*, **51**, e2023GL107298, https://doi.org/10.1029/2023GL107298.

Lew, J. K., D. C. Montague, H. R. Pruppacher, and R. M. Rasmussen, 1986: A Wind Tunnel Investigation on the Riming of Snowflakes. Part II: Natural and Synthetic Aggregates. *J. Atmos. Sci.*, **43**, 2410–2417, https://doi.org/10.1175/1520-0469(1986)043%3C2410:AWTIOT%3E2.0.CO;2.

Li, D., M. L. Wrzesien, M. Durand, J. Adam, and D. P. Lettenmaier, 2017: How much runoff originates as snow in the western United States, and how will that change in the future? *Geophys. Res. Lett.*, **44**, 6163–6172, https://doi.org/10.1002/2017GL073551.

Locatelli, J. D., and P. V. Hobbs, 1974: Fall speeds and masses of solid precipitation particles. *J. Geophys. Res.*, **79**, 2185–2197, https://doi.org/10.1029/JC079i015p02185.

Löffler-Mang, M., and J. Joss, 2000: An Optical Disdrometer for Measuring Size and Velocity of Hydrometeors. *J. Atmos. Oceanic Technol.*, **17**, 130–139, https://doi.org/10.1175/1520-0426(2000)017%3C0130:AODFMS%3E2.0.CO;2.

——, and U. Blahak, 2001: Estimation of the Equivalent Radar Reflectivity Factor from Measured Snow Size Spectra. *J. Appl. Meteorol. Climatol.*, **40**, 843–849, https://doi.org/10.1175/1520-0450(2001)040%3C0843:EOTERR%3E2.0.CO;2.

Long, A. B., A. W. Huggins, and B. A. Campistron, 1990: Investigations of a Winter Mountain Storm in Utah. Part I: Synoptic Analyses, Mesoscale Kinematics, and Water Release Rates. *J. Atmos. Sci.*, **47**, 1302–1322, https://doi.org/10.1175/1520-0469(1990)047%3C1302:IOAWMS%3E2.0.CO;2.

Maahn, M., and P. Kollias, 2012: Improved Micro Rain Radar snow measurements using Doppler spectra post-processing. *Atmos. Meas. Tech.*, **5**, 2661–2673, https://doi.org/10.5194/amt-5-2661-2012.

Majewski, A., J. R. French, and S. Haimov, 2003: Airborne Radar Doppler Spectrum Width as a Scale-Dependent Turbulence Metric. *J. Atmos. Oceanic. Technol.*, **40**, 1541–1555, https://doi.org/10.1175/JTECH-D-23-0056.1.

Marwitz, J. D., 1980: Winter Storms over the San Juan Mountains. Part I: Dynamical Processes. *J. Appl. Meteorol. Climatol.*, **19**, 913–926, https://doi.org/10.1175/1520-0450(1980)019%3C0913:WSOTSJ%3E2.0.CO;2.

Matrosov, S. Y., 2007: Modeling Backscatter Properties of Snowfall at Millimeter Wavelengths. *J. Atmos. Sci.*, **64**, 1727–1736, https://doi.org/10.1175/JAS3904.1.

McMurdie, L. A., A. K. Rowe, R. A. Houze, S. R. Brodzik, J. P. Zagrodnik, and T. M. Schuldt, 2018: Terrain-Enhanced Precipitation Processes Above the Melting Layer: Results From OLYMPEX. *J. Geophys. Res. Atmos.*, **123**, 12194–12209, https://doi.org/10.1029/2018JD029161.

Medina, S., and R. A. Houze, 2003: Air motions and precipitation growth in Alpine storms. *Q. J. R. Meteorol. Soc.*, **129**, 345–371, https://doi.org/10.1256/qj.02.13.

Meybeck, M., P. Green, and C. Vörösmarty, 2001: A New Typology for Mountains and Other Relief Classes. *Mount. Res. Dev.*, **21**, 34–45, https://doi.org/10.1659/0276-4741(2001)021%5B0034:ANTFMA%5D2.0.CO;2.

Meyers, M. P., and W. J. Steenburgh, 2013: Mountain Weather Prediction: Phenomenological Challenges and Forecast Methodology. *Mountain Weather Research and Forecasting: Recent Progress and Current Challenges*, F.K. Chow, S.F.J. De Wekker, and B.J. Snyder, Eds, Springer Netherlands, 1–34, https://doi.org/10.1007/978-94-007-4098-3_1.

Minder, J. R., T. W. Letcher, L. S. Campbell, P. G. Veals, and W. J. Steenburgh, 2015: The Evolution of Lake-Effect Convection during Landfall and Orographic Uplift as Observed by Profiling Radars. *Mon. Wea. Rev.*, **143**, 4422–4442, https://doi.org/10.1175/MWR-D-15-0117.1.

NCEI,: U.S. Climate Normals, accessed 5 April 2024, https://www.ncei.noaa.gov/products/land-based-station/us-climate-normals.

Neiman, P. J., F. M. Ralph, A. B. White, D. E. Kingsmill, and P. O. G. Persson, 2002: The Statistical Relationship between Upslope Flow and Rainfall in California's Coastal

Mountains: Observations during CALJET. *Mon. Wea. Rev.*, **130**, 1468–1492, https://doi.org/10.1175/1520-0493(2002)130%3C1468:TSRBUF%3E2.0.CO;2.

Pettersen, C., M. S. Kulie, L. F. Bliven, A. J. Merrelli, W. A. Petersen, T. J. Wagner, D. B. Wolff, and N. B. Wood, 2020: A Composite Analysis of Snowfall Modes from Four Winter Seasons in Marquette, Michigan. *J. Appl. Meteor. Climatol.*, **59**, 103–124, https://doi.org/10.1175/JAMC-D-19-0099.1.

Richter, J., C. Pettersen, D. Moisseev, J. Shates, and F. King, 2025: Macro- and Microphysical Properties of Atmospheric River Snowfall: Results from Two Instrument Sites. *J. Appl. Meteorol. Climatol.*, **64**, 1607–1627, https://doi.org/10.1175/JAMC-D-24-0220.1.

Roe, G. H., 2005: Orographic Precipitation. *Annu. Rev. Earth Planet. Sci.*, **33**, 645–671, https://doi.org/10.1146/annurev.earth.33.092203.122541.

Schultz, D. M., and R. J. Trapp, 2003: Nonclassical Cold-Frontal Structure Caused by Dry Subcloud Air in Northern Utah during the Intermountain Precipitation Experiment (IPEX). *Mon. Wea. Rev.*, **131**, 2222–2246, https://doi.org/10.1175/1520-0493(2003)131%3C2222:NCSCBD%3E2.0.CO;2.

Stark, D., B. A. Colle, and S. E. Yuter, 2013: Observed Microphysical Evolution for Two East Coast Winter Storms and the Associated Snow Bands. *Mon. Wea. Rev.*, **141**, 2037–2057, https://doi.org/10.1175/MWR-D-12-00276.1.

Steenburgh, J., M. L. Wasserstein, and P. G. Veals, 2025a: Alta-Atwater Micro Rain Radar Data 2022–2024, https://doi.org/10.7278/S5d-wern-v6kz.

——, ——, ——, A. Evans, and D. Kingsmill, 2025b: Alta Atwater PARSIVEL Disdrometer Measurements 2022–2024. The Hive: University of Utah Research Data Repository, accessed 10 June 2025, https://doi.org/10.7278/S5d-wtpn-az0j.

——, ——, ——, ——, and ——, 2025c: Highland PARSIVEL Disdrometer Measurements 2022–2024. The Hive: University of Utah Research Data Repository, accessed 10 June 2025, https://doi.org/10.7278/S5d-8vtz-5fsn.

Steenburgh, W. J., 2003: One Hundred Inches in One Hundred Hours: Evolution of a Wasatch Mountain Winter Storm Cycle. *Wea. Forecasting*, **18**, 1018–1036, https://doi.org/10.1175/1520-0434(2003)018%3C1018:OHIIOH%3E2.0.CO;2.

Stoelinga, M. T., R. E. Stewart, G. Thompson, and J. M. Thériault, 2013: Microphysical Processes Within Winter Orographic Cloud and Precipitation Systems. *Mountain Weather Research and Forecasting: Recent Progress and Current Challenges*, F.K. Chow, S.F.J. De Wekker, and B.J. Snyder, Eds, *Springer Atmospheric Sciences*, Springer Netherlands, 345–408, https://doi.org/10.1007/978-94-007-4098-3_7.

Utah Department of Transportation, 2022a: *Little Cottonwood Canyon, Environmental Impact Statement: Chapter 1, Purpose and Need*, accessed 5 April 2024.

——, 2022b: *Little Cottonwood Canyon, Environmental Impact Statement: Chapter 6, Economics*, accessed 5 April 2025.

Valdivia, J. M., P. N. Gatlin, S. Kumar, D. Scipión, Y. Silva, and W. A. Petersen, 2022: The GPM-DPR Blind Zone Effect on Satellite-Based Radar Estimation of Precipitation over the Andes from a Ground-Based Ka-band Profiler Perspective. *J. Appl. Meteor. Climatol.*, **61**, 441–456, https://doi.org/10.1175/JAMC-D-20-0211.1.

Veals, P. G., M. L. Wasserstein, and J. Steenburgh, 2025: Highland High Micro Rain Radar Data 2022–2024, https://doi.org/10.7278/S5d-n1jc-2d68.

Viviroli, D., and R. Weingartner, 2004: The hydrological significance of mountains: from regional to global scale. *Hydrol. Earth Syst. Sci.*, **8**, 1017–1030, https://doi.org/10.5194/hess-8-1017-2004.

Viviroli, D., H. H. Dürr, B. Messerli, M. Meybeck, and R. Weingartner, 2007: Mountains of the world, water towers for humanity: Typology, mapping, and global significance. *Water Resour. Res.*, **43**, https://doi.org/10.1029/2006WR005653.

Wasserstein, M., and J. Steenburgh, 2025: Alta-Collins Snow and Liquid Precipitation Equivalent Observations 2023-2024. Accessed 10 April 2025, https://doi.org/10.7278/S5d-dx7x-d8ay.

Wasserstein, M. L., and W. J. Steenburgh, 2023: Alta-Collins Snow and Liquid Precipitation Equivalent Observations 2000–2023. Accessed 12 September 2023, https://toi.lib.utah.edu/resolve/10.7278/S50d-nsy5-8bje.

Wasserstein, M. L., and W. J. Steenburgh, 2024: Diverse Characteristics of Extreme Orographic Snowfall Events in Little Cottonwood Canyon, Utah. *Mon. Wea. Rev.*, **152**, 945–966, https://doi.org/10.1175/MWR-D-23-0206.1.

Wood, V. T., R. A. Brown, and S. V. Vasiloff, 2003: Improved Detection Using Negative Elevation Angles for Mountaintop WSR-88Ds. Part II: Simulations of the Three Radars Covering Utah. *Wea. Forecasting*, **18**, 393–403, https://doi.org/10.1175/1520-0434(2003)18%3C393:IDUNEA%3E2.0.CO;2.

Xu, X., X. Chen, X. Zhao, D. Cao, Y. Liu, L. Li, and Y. Ma, 2023: Microphysical Characteristics of Snowfall on the Southeastern Tibetan Plateau. *J. Geophys. Res. Atmos.*, **128**, e2023JD038760, https://doi.org/10.1029/2023JD038760.

Yuter, S. E., and R. A. Houze, 1995: Three-Dimensional Kinematic and Microphysical Evolution of Florida Cumulonimbus. Part II: Frequency Distributions of Vertical Velocity, Reflectivity, and Differential Reflectivity. *Mon. Wea. Rev.*, **123**, 1941–1963, https://doi.org/10.1175/1520-0493(1995)123%3C1941:TDKAME%3E2.0.CO;2.

——, D. E. Kingsmill, L. B. Nance, and M. Löffler-Mang, 2006: Observations of Precipitation Size and Fall Speed Characteristics within Coexisting Rain and Wet Snow. *J. Appl. Meteor. Climatol.*, **45**, 1450–1464, https://doi.org/10.1175/JAM2406.1.

——, D. A. Stark, J. A. Crouch, M. J. Payne, and B. A. Colle, 2011: The Impact of Varying Environmental Conditions on the Spatial and Temporal Patterns of Orographic Precipitation over the Pacific Northwest near Portland, Oregon. *J. Hydrometeor.*, **12**, 329–351, https://doi.org/10.1175/2010JHM1239.1.